

Cusped Mass Density Profiles and Magnification Ratios of Double Image Gravitational Lenses

P. T. Mutka^{*}

University of Oulu, Department of Physical Sciences, Theoretical Physics Division, P.O. Box 3000, 90014 Oulun Yliopisto, Finland

Submitted 11 March 2009 for publication in MNRAS by the Royal Astronomical Society and Blackwell Publishing.

First revision 10 July 2009.

ABSTRACT

We have been able to connect the statistics of the observed double image gravitational lenses to the general properties of the internal structure of dark matter haloes. Our analytical theory for the GNFW lenses with parametrized cusp slope (α) gives us a relation connecting the cusp slope of the lensing profile to the observed magnification ratio of the produced images and location of the optical axis. The relation does not depend on cosmology, total lens mass, concentration or redshifts of the the lens and the lensed object. Simple geometry of axially symmetric lensing and aforementioned relation enables us to define a threshold value α_{CSL} for the cusp slope, independent from location of the optical axis. The threshold cusp slope value $\alpha = \alpha_{\text{CSL}}$ is the shallowest slope for the inner part of the GNFW profile that can produce the observed magnification ratio with any lensing configuration. We use distribution of these threshold values in a statistical study of the double image lenses in order to limit the possible cusp slope values, and identify whether there exists a population of haloes with similar profiles. Our theoretical fit indicates that within our sample of double image gravitational lenses, most of the haloes have cusp slope $\alpha = -1.95 \pm 0.02$. We have also found an indication of a second population of lenses with a cusp slope value $\alpha = -1.49 \pm 0.09$. We estimate that there is about 99 per cent probability that the observed feature in the threshold value limit distribution is produced by the second population of lenses, with their own characteristic density profile. The data indicating the exact characteristics of the sub-population is noisy. Roughly one out of six haloes within the sample belong to this shallower cusp slope group. We investigate errors in our analysis by constructing mock catalogues with the Monte-Carlo method.

Key words: gravitational lensing, relativity, methods: analytical, galaxies: haloes, cosmology: dark matter

1 INTRODUCTION

The large scale structure formation in the universe is dominated by the gravitational evolution of dark matter (DM) and the expansion of the universe (Peebles 1982; Blumenthal et al. 1984; Davis et al. 1985). Currently, the best candidate for the DM component is a weakly interacting massive particle (WIMP). A host of candidate particles can be suggested from the various extensions of the standard particle theory, for example supersymmetry (Ellis et al. 1991; Martin 1998) or Kaluza–Klein concepts (Cheng et al. 2002; Servant & Tait 2003).

Theories concerning structure formation usually postulate non-interacting dark matter that is affected only by gravity. Since the last decade, a large number of

studies employing analytical theories and/or N-body simulations have been conducted on this basis. There are also several variants of this approach, in which DM has been attributed with additional properties, such as being self-interacting (e.g. Spergel & Steinhardt 2000; Burkert 2000; Romeel et al. 2001; D’Onghia & Burkert 2003; D’Onghia, Firmani & Chincarini 2003, and references therein), decaying (e.g. Abdelqader & Melia 2008; Borzumati, Bringmann & Ullio 2008) or having a postulated equation of state (for example Austin et al. 2008).

At the linear regime, the current state-of-the-art cosmological theory, Λ CDM-model with inflation, is very successful and can explain most of the observations. However, problems arise at the nonlinear regime, where the DM halo is decoupled from the expansion of the universe and evolves through self-gravitation and gravitational in-

^{*} E-mail: Petri.Mutka@oulu.fi

interactions with its environment (Moore et al. 1998, 1999; Power et al. 2003).

At the high density region of dark matter halo cores, the physical properties of the dark matter particles and their interactions should become important. According to Spergel & Steinhardt (2000); Burkert (2000) the weak-interaction cross section of the dark matter particle can have significant effect on the shape of the density profile on cosmological time scales. The cross section has also been constrained by Randall et al. (2002) using the Bullet galaxy cluster. On the other hand, Beacom, Bell & Mack (2007) determine upper limit for the weak-interaction cross section from the cosmic diffuse neutrino background, and argue that dark matter haloes cannot be significantly altered by dark matter particle annihilations. It is clear, that observations and theoretical studies of dark matter haloes can help us narrow down the properties of the candidate particles.

The study of dark matter halo formation at the non-linear regime by Navarro et al. (1996, 1997) found that the dark matter haloes follow roughly a universal radially symmetric density profile (NFW). In the study, one halo consisted of several thousand gravitating DM-particles. Similar N-body experiments have been conducted regularly with increasing number of DM-particles and better resolution by several authors, see e.g. Moore et al. (1998, 1999); Ghigna et al. (2000).

Since then, several N-body study inspired models for the DM-haloes have been proposed. They all share some common properties; at the outer fringes, the halo follows $\rho \propto r^{-3}$ profile. After the transition region at scale radius r_s , the profile is changed to value $\rho \propto r^\alpha$ representing a cusped (or flat) core.

An ad hoc explanation for this behaviour is that the outer region is in the state of 'inflow', where the dark matter decouples from the general expansion of the universe, and streams towards the core region of the halo. This is characterized by dominating radial component of the velocity field. Inside the scale radius r_s , where the velocity field is more thermalized, the halo is composed of captured dark matter component that has passed through the core and turned back at least once. See for example Dehnen & McLaughlin (2005) or Hansen (2009) for further details.

In their study, Navarro et al. (1996, 1997) found an universal cusp slope $\alpha = -1$, valid for haloes at extensive range of size scales. More recent N-body studies have resulted an array of different slope values ranging from $\alpha = -1$ to $\alpha = -2$. This ambiguity in resolving the cuspidity of the DM haloes with N-body simulations, and contradicting observations from galactic dynamics has been one of the central weaknesses of the Λ CDM paradigm.

The observed shape of the density profile can be measured indirectly by analyzing internal dynamics and kinematics of nearby galaxies, measuring X-ray temperature profile, using Sunyaev-Zel'dovich effect, or with weak lensing measurements of galaxy clusters. Several authors has published results characterizing the profile shape by combining some of these observations, see e.g. Mahdavi et al. (2007) and references therein.

These studies either assume a profile shape in advance or try to acquire a fit for it. In both cases, the NFW profiles ($\alpha \sim -1.0$) have proven successful (Gavazzi 2005; Pointecouteau, Arnaud & Pratt

2005; Vikhlinin et al. 2006; Limousin et al. 2008), although shallower density profiles $\alpha \sim -0.5$ have been reported (Sanderson, Finoguenov & Mohr 2005; Voigt & Fabian 2006). On the other hand, lensing studies by Sereno, Lubini & Jetzer (2009) estimated slightly steeper density profile for the cluster AC114 than the canonical NFW value.

Rotation curves and analysis of dynamics for late type spiral galaxies indicate that they must have shallower non-cusped cores (Valenzuela et al. 2007; Donato et al. 2009). If a galaxy has a bar, it will interact with the halo and this should slow-down the bar rotation, see e.g. Weinberg (1985). It has been claimed that bars rotate so fast (corotation resonance close to bar radius) that they could not be embedded into strongly concentrated halos. On the other hand, the interaction between the bar and halo have been suggested to make the cusp more shallow (Debattista & Sellwood 2000). However, there seems to be possible issues with the resolution of N-body models (Weinberg & Katz 2007), see also Sellwood (2008).

Interestingly, in recent high resolution N-body models by Dubinski, Berentzen & Shlosman (2009), the bar stayed fast and did not destroy the cusp. Further complications are provided by recent results indicating that some small bars rotate slowly (Rautiainen, Salo & Laurikainen 2008; Chemin & Hernandez 2009). Slow rotation for such bars was suggested already by Elmegreen & Elmegreen (1985) on morphological grounds, so it is possible that their origin is somehow different from larger bars that are studied more frequently.

The dwarf galaxies at low surface brightness are considered as being dominated by dark matter component. However, direct measurements of the rotation curves of these objects indicate a constant density core without a cusp, see Burkert (1995) or Zackrisson et al. (2006), and corresponding references therein.

The newest development in the constraints for the dark matter halo profiles comes from the observational particle physics. The WMAP probe has observed a microwave "haze" around the Galactic core. This can be explained by hypothetical dark matter particles annihilating at the high density region of the Milky Way core. The "haze" is interpreted as emitted synchrotron radiation from the produced electron-positron pairs, and it matches predicted emission from a dark matter halo with a cusped profile, $\rho \propto r^{-1.2}$ within the inner kiloparsecs (Hooper, Finkbeiner & Dobler 2007). Since there is no definite direct detection of the dark matter particle to date, this can be considered as a hypothetical scenario yet to be proved or disproved.

The largest coherent sample of the galaxy scale strong gravitational lenses has been measured with the HST in the Sloan Lens ACS survey (Bolton et al. 2006). Gavazzi et al. (2007) made a statistical study about subset of these lenses, and confirmed that on average, an isothermal profile $\alpha \sim -2$ fits the lensing profiles. Several strong gravitational lensing studies have also suggested shallower cusp slopes (Sand, Treu & Ellis 2002; Sand et al. 2004) at $\alpha \sim -0.5$.

However, flat profiles have severe problems in strong lensing. In our previous paper Mutka & Mähönen (2006), we developed a semi-analytical theory for axially symmetric gravitational lensing and employed it to the generalization of the NFW profile (GNFW), by Navarro et al. (1996, 1997);

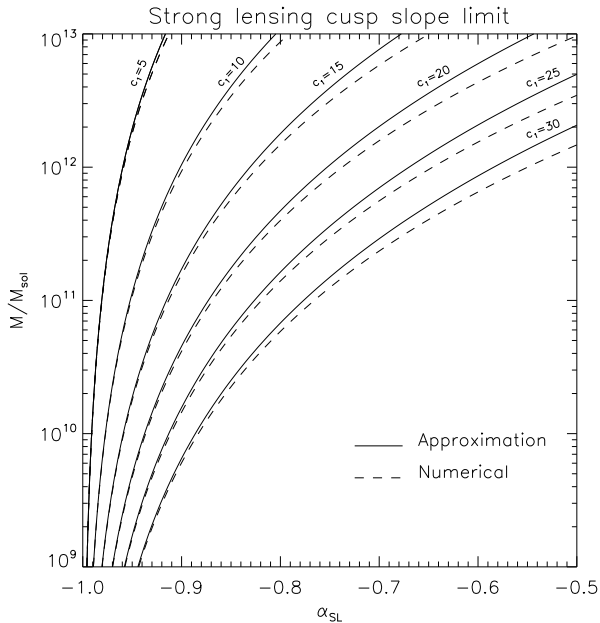


Figure 1. The strong lensing condition, equation (2) is function of the mass M of the lens. This plot shows the required mass for the lens as a function of the strong lensing cusp slope limit α_{SL} . The strong lensing is not possible on the right hand side (below) of each curve. The curves with concentration parameter values $c_1 = 5, 10, 15, 20, 25, 30$ are plotted for the lens at redshift $z = 0.3$, and the source at redshift $z = 1.0$. The dashed line is a numerical version of the condition approximated by equation (2) as prescribed in the appendix A.

Zhao (1996). In the GFW profile, value of the cusp slope is a free parameter:

$$\rho \propto r^\alpha (1+r)^{-3-\alpha}. \quad (1)$$

Note that we use convention in which the cusp slope α has negative values. In axial lensing context, the GFW halos with cusp slope shallower than $\alpha \sim -1$ have severe problems in strong lensing (Mutka & Mähönen 2006).

The cusp slope limit for strong lensing α_{SL} is a function of the cosmological parameters, lensing geometry, lens mass and lens concentration. Basically, at this limit the radius of the Einstein ring for a GFW lens goes to zero, after which the strong lensing configurations become impossible. A good approximation for this limit is

$$\alpha_{\text{SL}} = -\frac{3}{2} + \frac{1}{2} \sqrt{1 + \frac{1600 r_s \rho_{\text{cr}} c_1^3 (1+c_1)}{3 \Sigma_{\text{cr}} [(1+c_1) \log(1+c_1) + c_1]}}, \quad (2)$$

that produces values slightly above the $\alpha \sim -1$, with reasonable lens masses and concentrations. Figure 1 shows the required lens mass as function of the strong lensing condition, calculated with equation (2) and corresponding fully numerical solution. With usual lens masses order of $M \sim 10^{12} M_\odot$, the strong lensing is limited close to $\alpha \sim -1$. Only excessive concentration allows lens systems with slope $\alpha \sim -0.5$ that can produce multiple images. Appendix A presents definitions of r_s , ρ_{cr} and Σ_{cr} and derivation for the equation (2).

It can also be shown that, if dark matter haloes have shallower profile ($\alpha \geq -1.5$), triple image lenses with visible

inner caustic image should be very common. The estimated probability for a triple image lens configuration is

$$P_{\text{triple}}(\alpha) = 1 - \frac{\alpha^2}{4}, \quad (3)$$

and there are only three observed lens systems with (suspected) visible inner caustic image out of one hundred. This gives an average cusp slope value $\alpha \sim -1.97$, which is closer to the isothermal value. See section 2.1 for derivation of the equation (3) and further details. Note that equations (2) and (3) are also valid with reasonable values of eccentricity for elliptic lens haloes. See section 2 for further discussion.

We investigate the characteristics of the lensing profiles by deriving a cusp slope limit (CSL) value α_{CSL} for the shallowest cusp slope, that can produce the required flux difference for the images with any lensing geometry (i.e. it must hold $\alpha < \alpha_{\text{CSL}}$ for the lensing profile). We assume random alignments for the sources, and use the CSL value in statistical analysis of the double image lenses. By examining distribution of these threshold values, we can characterize the general properties of lensing profiles. For this purpose, we composed a catalogue of the double image lenses exhibiting properties of radial symmetry. Our sample is based on the known cases of the lensed quasars listed in CASTLES survey.

Our method relies on the observed flux ratios of double image lenses. Because we use image flux ratios, information on the lens and source redshifts, lens mass and concentration, and cosmology is not required. With our formulation, the intrinsic halo properties are separated from these quantities. Therefore, the statistical method does not require theoretical distributions characterizing lens and source populations (such as Schechter function coupled with the mass-luminosity relation for lenses, or quasar luminosity functions for sources), which makes it possible to avoid number of different uncertainties in the analysis.

However, there are several factors that can corrupt the observed fluxes from the predicted magnification produced by the lens. We examine effects by the lens ellipticities, the substructure in the lensing halo and time-delay from a variable source. This is done by constructing mock lens catalogues with the Monte Carlo method when accounting for these factors.

The next section presents a brief review of our lensing theory, formulation for the CSL value, triple image lens probability and description for theoretical CSL distribution. The third section describes the selected lens systems and the catalogue used in the study. The Monte Carlo testing of the CSL statistics is presented in section four. Finally, we employ the statistical CSL analysis on real double image lens data in section five. The last section contains conclusions and discussion regarding the study. The derivation for the cusp slope limit for strong lensing is presented in appendix A.

2 THEORY

Here we briefly review the relevant lensing theory presented in our previous paper (Mutka & Mähönen 2006), and derive the cusp slope limit (CSL) value. The CSL value is based on

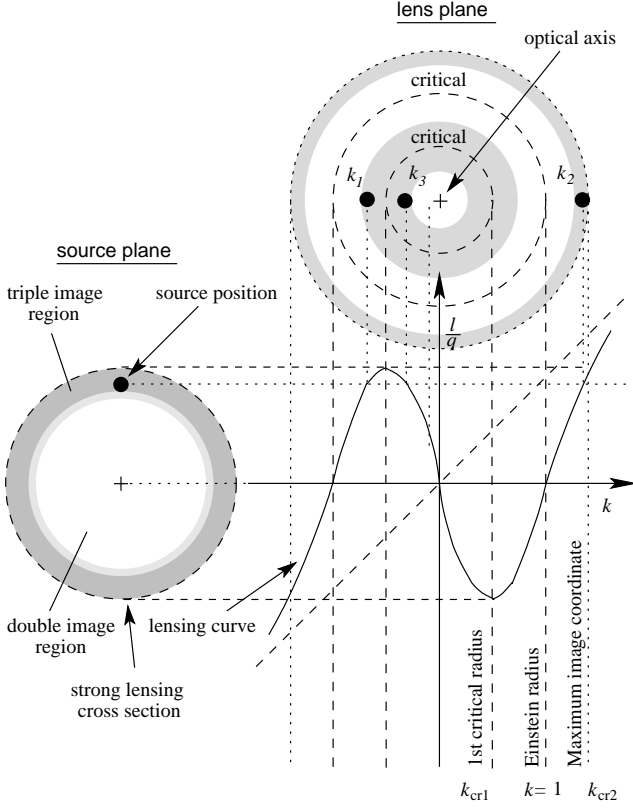


Figure 2. The lens equation normalized with the Einstein radius (4) produces three images k_1 , k_2 and k_3 . The first image k_1 is located between the Einstein radius ($l/q = 0$ or $k = 1$) and the first critical radius $k = \nu$. The second image is at the opposite side of the optical axis, between the Einstein radius and the second critical radius, equation (5) (the largest possible distance from the optical axis for the multiple imaged source). The third image k_3 (inner image) is inside the first critical radius, and it is usually strongly demagnified. With large values of k , outside the second critical radius, the lensing curve should approach to $l/q = k$. The chosen lensing curve strongly exaggerates size of the triple image region.

the analytical formulation of the magnification ratio of the lensed images, and its solutions.

In gravitational lensing, the source image is lensed by the gravitational field of the lens object. The source image that is thought to be confined on a plane at the source distance D_s , produces observed images on the lens plane (at the lens object distance D_L). Mapping from the source plane to the lens plane is described by the lens equation.

In axially symmetric lensing, we choose the line connecting the observer and the lens as origin for the frame of reference. Corresponding radial coordinate at the source plane is denoted with y and at the lens plane with x , as in Schneider, Ehlers & Falco (1992).

When the source is located at the origin ($y = 0$), it is mapped to the lens plane as an Einstein ring, that has radius $x = x_e$. The axially symmetric lens equation for the GFW density profile, normalized with the Einstein radius x_e , can be written as

$$l = \begin{cases} qk(1 - |k|^{\alpha+1}) & \text{if } \alpha \neq -1, -2 \leq \alpha < 0 \\ \frac{\mu_0}{2} k \log |k| & \text{if } \alpha = -1 \end{cases}, \quad (4)$$

where the radial coordinate at the source plane is $l = y/(x_e r_s)$ and corresponding radial coordinate at the lens plane is $k = x/x_e = r/(r_s x_e)$. Scale radius r_s , and constants q and μ_0 depend on the cosmology, the mass and the concentration of the lens object, and the geometrical setup of the lensing. Note that our cusp slope value is a negative number. The exact definition for the scale radius r_s and the corresponding unnormalized lens equation can be found in appendix A and paper Mutka & Mähönen (2006).

With this notation, the Einstein radius is located at $k = 1$. The first critical radius at $k_{cr1} = \nu = (\alpha + 2)^{-1/(\alpha+1)}$ and the corresponding twin image at the opposite side of the lens has a good approximation

$$k_{cr2} = \frac{\alpha + 1 + \sqrt{1 + 2\nu}}{\alpha + 2}. \quad (5)$$

The critical radii ($k = 1$ and $k = k_{cr1} = \nu$) are connected to the caustic curves where the magnification diverges, see figure 2, or Mutka & Mähönen (2006) for further details. Note that although the image at k_{cr1} is at the critical curve, the corresponding twin image at k_{cr2} is not.

The approximation in the lens equation (4) breaks down with large values of the radial coordinate k , and therefore the lens equation (4) does not behave asymptotically as it should. This asymptotic behaviour can be corrected by writing the lens equation ($\alpha \neq -1$) piece-wisely as

$$l = \begin{cases} qk(1 - |k|^{\alpha+1}), & \text{when } k \leq k_B \\ k - \frac{\alpha+1}{\alpha+3} \frac{k_B^2}{k} (1 - q), & \text{when } k > k_B \end{cases}, \quad (6)$$

where the lens equation (6) is divided at

$$k_B = \left(\frac{2(q-1)}{q(\alpha+3)} \right)^{1/(\alpha+1)} \quad (7)$$

in order to avoid negative surface densities.

A lensed image at location $k \leq k_B$ is magnified by the lens as

$$\mu = q^{-2} |1 - |k|^{\alpha+1}|^{-1} |1 - (\alpha+2)|k|^{\alpha+1}|^{-1}, \quad \alpha \neq -1. \quad (8)$$

Note, that the factor q dependency is contained into a coefficient multiplying the magnification. Therefore, the q dependency is cancelled out when considering ratio of image magnifications in strong lensing cases.

The positive definitive lensed images at k_1 , k_2 and k_3 that are solutions of the lens equation (4) or (6), are labelled as in figure 2. The image closest to the source, that has positive parity, is located at k_2 . The images at k_1 and k_3 are at the opposite side of the lens with negative and positive parities (the image at k_3 is usually strongly demagnified). The solutions k_1 and k_2 of a source at l in the lens equation must satisfy

$$\frac{k_1^{\alpha+2} + k_2^{\alpha+2}}{k_1 + k_2} = 1, \quad \text{when } \alpha \neq -1. \quad (9)$$

Now we can parameterize the lens equation with coordinate ratio $\theta = k_1/k_2 = x_1/x_2 = \theta_1/\theta_2 \leq 1$, where θ_1 and θ_2 are observed angular distances of the images from the optical axis on the sky correspondingly. The advantage of the parameter θ is that it is directly observable, if the location of the optical axis is known.

The ratio of the image coordinates $\theta = k_1/k_2$ has a minimum value at

$$\theta = \theta_{\min} = \frac{k_{\text{cr1}}}{k_{\text{cr2}}} = \frac{\nu(\alpha + 2)}{\alpha + 1 + \sqrt{1 + 2\nu}} \quad (10)$$

corresponding to the most asymmetric configuration for the strong lensing for a source image at $l = l_{\max}$. If the image coordinate ratio θ is decreased below this value, it describes the ratio $\theta = k_3/k_2$ for the demagnified inner caustic image. Thus, θ_{\min} is also the smallest value for the $\theta = k_1/k_2$.

When relation (9) is employed, and $\alpha \neq -1$, the image coordinates become

$$\begin{aligned} k_1 &= \theta \left[\frac{1+\theta}{1+\theta^{\alpha+2}} \right]^{1/(\alpha+1)} \\ k_2 &= \left[\frac{1+\theta}{1+\theta^{\alpha+2}} \right]^{1/(\alpha+1)} \end{aligned} \quad (11)$$

and the lens equation can be written as

$$l = q\theta \left[\frac{1+\theta}{1+\theta^{\alpha+2}} \right]^{1/(\alpha+1)} \frac{\theta^{\alpha+1} - 1}{\theta^{\alpha+2} + 1}, \quad \alpha \neq -1, \quad k < k_B. \quad (12)$$

Now the magnification ratio M of the lensed images as a function of the cusp slope α and ratio of the image coordinates $\theta = k_1/k_2$ becomes

$$\begin{aligned} M(\alpha, \theta) &= \frac{\mu_1}{\mu_2} \\ &= \theta \frac{|\theta^{\alpha+2} + 1 - (1+\theta)(\alpha+2)|}{|\theta^{\alpha+2} + 1 - \theta^{\alpha+1}(1+\theta)(\alpha+2)|}, \quad \alpha \neq -1, \quad k < k_B \end{aligned} \quad (13)$$

as presented in Mutka & Mähönen (2006). Note that the derived relation (13) between the location of the optical axis, the image magnification ratio and the value of the cusp slope does not depend on the mass or the concentration of the lens, the cosmological model, or the redshifts of the source and lens object. This makes it an ideal tool for studying the structure of the lensing halos by separating their intrinsic properties from the extrinsic lensing conditions.

When the magnification (flux) ratio of the observed images (M_0) is measured, the location of the optical axis (θ) as a function of the cusp slope parameter α can be solved from equation (13). Basically, there are two different groups of solutions corresponding to triple and double image lens configurations.

If the solutions are plotted at (α, θ) -plane, the double image solutions vanish at $\alpha = \alpha_{\text{CSL}}$ and $\theta = \theta_{\text{CSL}}$, where

$$\left. \frac{dM}{d\theta} \right|_{\substack{\theta = \theta_{\text{CSL}} \\ \alpha = \alpha_{\text{CSL}}}} = 0. \quad (14)$$

This means that the double image solutions are restricted to cusp slopes $\alpha \in [-2, \alpha_{\text{CSL}}]$. But on the other hand, using the relation (13), this point can be related to the observed magnification ratio with

$$M(\alpha_{\text{CSL}}, \theta_{\text{CSL}}) = M_0. \quad (15)$$

Pair of equations (14) and (15), can be used to solve θ_{CSL} and α_{CSL} for a lens system with observed magnification ratio $M_0 = \mu_1/\mu_2 = F_1/F_2$ (where F_1 and F_2 are corresponding observed fluxes for the images). See figure 3.

At the configuration $(\alpha_{\text{CSL}}, \theta_{\text{CSL}})$, the lens has just enough 'power' to produce the magnification difference for the observed flux ratio. For shallower cusp slope values $\alpha > \alpha_{\text{CSL}}$ the observed flux ratio cannot be reached with any double image configuration.

The absolute maximum for the possible values of the

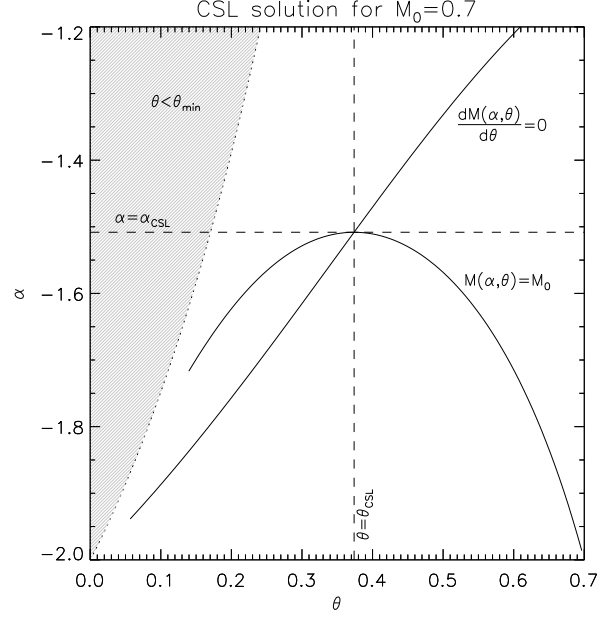


Figure 3. The CSL solution for a double image lens system with image flux ratio $M(\alpha, \theta) = M_0 = 0.7$, as calculated from equations (14) and (15). Horizontal axis shows coordinate ratio $\theta = k_1/k_2$ and vertical axis profile slope α . Curve $dM/d\theta = 0$ intersects the magnification ratio solutions $M(\alpha, \theta) = M_0$ at the shallowest possible cusp slope value $\alpha = \alpha_{\text{CSL}}$. The shaded area corresponds to the inner image solutions, where k_1 is replaced by k_3 , and triple image solutions are limited nearby $\theta = \theta_{\min}$.

cusp slope α can be calculated from the measured flux ratio for each observed double image lens system. This is the previously discussed cusp slope limit, abbreviated as CSL. When we assume random lensing alignments, the distribution of the CSL values depend only on the properties of the lensing profiles. For a single universal cusp slope value, the numerical formulation for the CSL probability is presented in section 2.2.

2.1 Condition for triple image lensing

An axially symmetric lens potential produces visible triple image lens when images at k_1 and k_3 are sufficiently close to the radial critical curve at $k_{\text{cr1}} = \nu$. Otherwise, the image k_3 inside the caustic curve becomes unobservable because of strong demagnification, while image k_1 remains magnified, and a double image lens system is observed.

Images nearby the critical radius k_{cr1} are produced by source images that are located near $l \sim l_{\max}$, where l_{\max} is the maximum source coordinate for producing multiple images (strong lensing). Thus, the triple image condition demarcates out part of the strong lensing region. In other words, for double image lensing, the source coordinate l must have $l < l_{\text{triple}} < l_{\max}$.

The condition for triple image lensing can be derived by examining the magnification ratio μ_1/μ_3 of the images k_1 and k_3 . This is done by expanding the lens equation at $k = \nu$, setting the condition $\mu_1/\mu_3 < \tau$ and solving it for the corresponding source coordinate. Here τ is the limiting value for the observable magnification ratio.

From the lensing theory presented in Mutka & Mähönen (2006), the maximum source coordinate has value

$$L_{\max} = \left(\frac{l}{q}\right)_{\max} = -\frac{\alpha+1}{\alpha+2}\nu, \quad (16)$$

where $\nu = (\alpha+2)^{-1/(\alpha+1)}$ and α is the cusp slope of the density profile in equation (1).

We normalize the lens equation

$$\frac{l}{q} = k(1 - |k|^{\alpha+1}) \quad (17)$$

with expression (16) in case of $-2 \leq \alpha < -1$. Now the lens equation can be expressed in new coordinates $y = l/(qL_{\max})$ and $x = k/\nu$ as

$$y = \frac{x}{\alpha+1}(\alpha+2 - x^{\alpha+1}). \quad (18)$$

We continue our derivation by expanding the re-normalized lens equation at $k = k_{\text{cr1}} = \nu \Leftrightarrow x = 1$, which gives us

$$y \approx 1 - \frac{\alpha+2}{2}(x-1)^2. \quad (19)$$

By solving this approximation we get the image location

$$x = 1 \pm \sqrt{2\frac{1-y}{\alpha+2}} \quad (20)$$

from a source nearby the critical curve. Here the positive sign corresponds to image k_1 and negative to k_3 . Again, from the lensing theory presented in Mutka & Mähönen (2006), the magnification ratio condition for the triple image lensing can be expressed as

$$\frac{\mu_1}{\mu_3} = \left(\frac{x_1}{x_3}\right)^2 \frac{|y-x_3|}{|y-x_1|} < \tau. \quad (21)$$

By inserting solutions for x_1 and x_3 from equation (20) to this expression and solving for the source coordinate y , the condition for observable triple image lensing becomes

$$y > 1 - \frac{\alpha+2}{2} \left(\frac{\tau-1}{\tau+1}\right)^2. \quad (22)$$

The power of two factor in parenthesis that depends on τ , approaches very quickly to the unit value if demanding ten or a hundredfold magnification ratio for the limit of observability. Because determining the exact value for the magnification ratio limit is impossible, we set this factor equal to one. Thus, practically without any loss of accuracy, the source image condition for the triple image lensing can be generalized to

$$y > -\frac{\alpha}{2} \Leftrightarrow \frac{l}{q} > \frac{\alpha\nu}{2} \frac{\alpha+1}{\alpha+2} = \frac{l_{\text{triple}}}{q}. \quad (23)$$

As before, we assume that the source images are uniformly distributed at the source plane inside radius L_{\max} . Now the source image coordinate limit (23) leads directly to a simple graphical probability for triple image lensing

$$P_{\text{triple}}(\alpha) = 1 - \frac{\alpha^2}{4}. \quad (24)$$

that depends only on the cusp slope parameter of the density profile (1). The expression (24) for probability of the triple image lensing can be considered also valid with reasonable values of ellipticities for triaxial haloes. Corresponding

treatment can be made for haloes with elliptic isocontours following the profile (1). Note, that the probability (24) applies only on proportional share of triple image lenses among already identified lens systems, not on arbitrary galaxy in the Universe. This is why the q term dependency vanishes from the equation. Additionally, this result does not account for the finite angular resolution in the real world observations.

The remarkably simple condition (23) and probability (24) have direct consequences on the general properties of the lensing potential and properties of dark matter haloes. According to the expression (24), double image lensing and triple image lensing have equal probability when $\alpha = \alpha_{\text{eq}} = -\sqrt{2} \sim -1.4$. If the cusp slope value $\alpha > \alpha_{\text{eq}}$, triple image lenses are more common than double image lenses. The fact that there are only three known cases with visible inner caustic image out of roughly hundred implicates that the cusp slope in the dark matter profile must be closer to isothermal value $\alpha \sim -2$ than α_{eq} .

In fact, if we set $P_{\text{triple}} = N_{\text{triple}}/N = 0.03$ and solve the cusp slope parameter from the equation (24), we get $\alpha \approx -1.97$ - a result rather close to the quoted value for the population H1 in this paper.

2.2 Theoretical CSL probability

Here we show how to calculate a numerical probability function for the CSL limit values. We assume that the source images are uniformly distributed at the double image region of the source plane limited by the equation (23), i.e. the radial source coordinate

$$y = \frac{l}{qL_{\max}} < -\frac{\alpha}{2} \leq 1. \quad (25)$$

We assume a single population of lenses with a universal cusp slope value α . All the slope parameters used in the following calculations have $-2 < \alpha < -1$. Special cases $\alpha = -1$ and $\alpha = -2$ could be treated in similar way, but it is not necessary at this point.

The differential probability for having a lens with value α_{CSL} is corresponding to an area of a ring with an inner radius y and an outer radius $y + dy$:

$$dP = 8\frac{y}{\alpha^2}dy, \quad (26)$$

where $y = y(\alpha_{\text{CSL}}; \alpha)$. This equation can be integrated in order to estimate the probability of a double image lens to have $\alpha_2 < \alpha_{\text{CSL}} < \alpha_1$:

$$P(\alpha_2 < \alpha_{\text{CSL}} < \alpha_1) = 4\frac{y^2(\alpha_2; \alpha) - y^2(\alpha_1; \alpha)}{\alpha^2}. \quad (27)$$

Although it could be possible to write an approximation for the function $y = y(\alpha_{\text{CSL}}; \alpha)$ or rewrite the differential (26) using other variables, we calculate it here numerically. For this purpose we employ the magnification ratio $M = M(\alpha, \theta)$ of the images k_1 and k_2 produced by the source image at l , as presented in equation (13). Here $\theta = k_1/k_2$ is the image coordinate ratio.

We start calculating the $y(\alpha_{\text{CSL}}; \alpha)$ for each α_{CSL} by solving the equation

$$\left. \frac{dM}{d\theta} \right|_{\substack{\alpha = \alpha_{\text{CSL}} \\ \theta = \theta_{\text{CSL}}}} = 0 \quad (28)$$

numerically for θ_{CSL} . The acquired value is subsequently inserted to

$$M(\alpha_{\text{CSL}}, \theta_{\text{CSL}}) = M(\alpha, \theta), \quad (29)$$

which is then solved numerically for θ . Equation (29) has two solutions $\theta = \theta_{(u)}(\alpha_{\text{CSL}})$ and $\theta = \theta_{(d)}(\alpha_{\text{CSL}})$. When these solutions are inserted into the lens equation

$$y = y(\theta, \alpha) = \frac{\theta}{L_{\text{max}}} \left[\frac{1 + \theta}{1 + \theta^{\alpha+2}} \right]^{1/(\alpha+1)} \frac{\theta^{\alpha+1} - 1}{\theta^{\alpha+2} + 1}, \quad (30)$$

source coordinate values $y_{(u)}(\alpha_{\text{CSL}}; \alpha)$ and $y_{(d)}(\alpha_{\text{CSL}}; \alpha)$ are acquired. Because we must limit the solutions to the double image cases, resulting $y_{(u)}$ or $y_{(d)}$ values are not allowed to exceed the limit (23).

With these two solutions, the probability (27) becomes

$$P(\alpha_2 < \alpha_{\text{CSL}} < \alpha_1) = \frac{4}{\alpha^2} \frac{y_{(d)}^2(\alpha_2; \alpha) - y_{(d)}^2(\alpha_1; \alpha) + y_{(u)}^2(\alpha_2; \alpha) - y_{(u)}^2(\alpha_1; \alpha)}{1}. \quad (31)$$

3 DOUBLE IMAGE LENS SYSTEMS

For this study, we composed a catalogue of double image lens systems, which have a configuration resembling axially symmetric lensing. The catalogue is based on JVAS-CLASS radio survey and optical CASTLES survey and it contains 44 lens systems, see table 1 and relevant references. Four of these systems had no data available during the conducted background research, which reduces number of useful systems down to 40.

The Jodrell Bank - VLA Astrometric Survey (JVAS, Patnaik et al. 1992; Browne et al. 1998; Wilkinson et al. 1998) and the Cosmic Lens All Sky Survey (CLASS, Jackson et al. 1995; Myers et al. 1995) were originally geared towards finding new gravitationally lensed systems in order to determine the value of the Hubble's constant H_0 . During the surveys, they observed roughly 10000 flat spectrum radio sources. At the moment these surveys has detected 20 strong lens systems. The CfA-Arizona Space Telescope LENS Survey is an ongoing HST survey of all the known strong lenses and lens candidates. The main goal of the survey is to create a uniform high quality photometric sample of these objects (Muñoz et al. 1998).¹

Our subsample of these surveys was chosen according to the following criteria: the lens system must have two clearly separate lensed images corresponding to a quasar source. Triple and quad lenses, Einstein rings and clearly non-axially-symmetric cases were excluded. Additional lensed components, such as radio jets were allowed as long as the lensed point source was present.

Table 1 summarizes properties of the accepted lens systems. After the name of the lens system, absence of a lens object candidate is indicated by a '-' in the second column of the table. If there are additional components at the immediate surroundings of the lens system, it is indicated with a 'x' in the third column. All the available flux measurements

from radio and optical observations were used to calculate mean flux ratio weighed with measurement errors in observations (columns four and five). The flux ratio is calculated by dividing the closer (dimmer) image flux with the further (brighter) image flux. Columns six and seven contain evaluation for redshifts of the lens candidate (if present) and the source correspondingly. The eighth and ninth columns in the table contain radio and optical cusp slope limit values (α_{CSL}). Note, that these may have different values because the radio and optical sources have different locations at the source plane. The last column lists the relevant references pointing to the source of the data and/or the publication reporting the discovery of the lens system.

After the preliminary Monte Carlo testing, we will use the calculated CSL values in the final statistical analysis. Because the optical data is more abundant, we have chosen to prefer optical values, and use radio measurements only if the optical data is not available.

4 MONTE CARLO TESTING

In order to test the CSL-analysis method against different perturbations and investigate the error sources, we have developed a computer code that generates mock lens catalogues. Our code uses rejection method with base distributions that are randomly sampled for initial redshifts, lens masses and source luminosities. Sampled values are fed to the lens equation solver that accounts for the lens asymmetries and other more sophisticated properties of the lensing event. Generated lens system is accepted or rejected according to the observed configuration, selected magnitude limit and minimum image separation threshold.

We use differential optical depth $\frac{d\tau}{dz}(M_L, z_s)$, as a function of lens mass M_L and source redshift z_s for the base lens distribution (Ofek, Rix & Maoz 2003). Our generator uses similar morphological mix for the lens galaxies, and we have chosen parameter values $U = -0.20$, $P = 1.20$ and $f_E = 0.95$ for the distribution. See Ofek, Rix & Maoz (2003) for further details, and information on other parameters affecting the distribution.

The source objects are sampled from a double power law luminosity function $\Phi(L, z_s)$ of quasars as presented by Wyithe & Loeb (2002). They use a luminosity function with pure luminosity evolution and additional break for very high redshift objects. See Wyithe & Loeb (2002) for further details.

Our parameters generate reasonably good samples of lens systems, as can be seen from figure 4. We compare our mock data against observed redshift distribution of lenses, redshift distribution of sources, image separations and lens masses inferred from the Faber-Jackson relation. We use Kolmogorov-Smirnov two-sample test providing a probability that the samples are drawn from the same background distribution. When observed lens object magnitudes are converted to absolute luminosities for mass estimation, evolutionary and K-corrections are applied to the data as presented by Poggianti (1997) and Bicker et al. (2004). Note, that the size of the observational sample is changing in each panel. The reason for this is that we use all the double image lens data available for testing, and some lens systems have missing data.

¹ C.S. Kochanek, E.E. Falco, C. Impey, J. Lehar, B. McLeod, H.-W. Rix, the CASTLES survey has a website <http://www.cfa.harvard.edu/castles/>

Table 1. Double image lens systems used in the study.

System	lens	gal	radio μ_1/μ_2	optical μ_1/μ_2	z_L	z_S	radio α_{CSL}	optical α_{CSL}	references
HE0047-1756				0.27 ± 0.02	0.41	1.66		-1.848 ± 0.010	Wisotzki et al. (2004)
HST01247+0352	-								Ratnatunga, Griffiths & Ostrander (1999)
HST01248+0351	-								Ratnatunga, Griffiths & Ostrander (1999)
Q0142-100				0.122 ± 0.003	0.49	2.72		-1.934 ± 0.002	Surdej et al. (1988); Lehar et al. (2000)
QJ0158-4325				0.3477 ± 0.0013		1.29		-1.7941 ± 0.0009	Morgan et al. (1999)
SDSS0246-0825				0.322 ± 0.007		1.68		-1.811 ± 0.004	Inada et al. (2005)
CLASS B0445+123	-		0.152 ± 0.005		0.557		-1.917 ± 0.003		Argo et al. (2003)
HE0512-3329	-			0.90 ± 0.07	(0.93)	1.57		-1.24 ± 0.12	Wucknitz et al. (2003)
CLASS B0631+519		x	0.129 ± 0.005		0.09/0.62		-1.930 ± 0.003		York et al. (2005)
CLASS B0739+366			0.171 ± 0.011	0.083 ± 0.011			-1.906 ± 0.006	-1.956 ± 0.006	Marlow et al. (2001)
HS0818+1227				0.145 ± 0.010	0.39	3.115		-1.921 ± 0.006	Hagen & Reimers (2000)
CLASS B0827+525	-		0.374 ± 0.002	0.06 ± 0.02		3.87	-1.7758 ± 0.0015	-1.967 ± 0.009	Koopmans et al. (2000)
CLASS B0850+054	-		0.164 ± 0.004		0.59	1.14/3.93?	-1.910 ± 0.002		Biggs et al. (2003)
SDSS0903+5028				0.477 ± 0.012	0.388	3.605		-1.702 ± 0.009	Johnston et al. (2003)
SBS0909+523				0.80 ± 0.03	0.83	1.38		-1.40 ± 0.03	Lehar et al. (2000)
RXJ0921+4529				0.215 ± 0.008	0.31	1.65		-1.880 ± 0.005	Muñoz et al. (2001)
FBQ0951+2635			0.2143 ± 0.0015	0.306 ± 0.010	(0.24)	1.24	-1.8799 ± 0.0010	-1.822 ± 0.006	Schechter et al. (1998)
BRI0952-0115				0.289 ± 0.005	(0.41)	4.50		-1.833 ± 0.003	Lehar et al. (2000)
Q0957+561			0.757 ± 0.005	0.94 ± 0.03	0.36	1.41	-1.449 ± 0.005	-1.19 ± 0.06	Greenfield, Roberts & Burke (1985)
SDSS1001+5027		x		0.740 ± 0.005		1.84		-1.466 ± 0.006	Oguri et al. (2005)
J1004+1229	-		0.44 ± 0.05	0.23 ± 0.04	0.95	2.65	-1.73 ± 0.04	-1.87 ± 0.02	Lacy et al. (2002)
Q1017-207				0.138 ± 0.004	(0.78)	2.55		-1.925 ± 0.002	Surdej et al. (1997); Lehar et al. (2000)
SDSS1021+4913		x		0.40 ± 0.03		1.72		-1.76 ± 0.02	Pindor et al. (2006)
JVAS B1030+074			0.0659 ± 0.0014	0.0280 ± 0.0008	0.60	1.54	-1.9654 ± 0.0008	-1.9857 ± 0.0004	Xanthopoulos et al. (1998); Lehar et al. (2000)
HE1104-1805				0.241 ± 0.009	0.73	2.32		-1.863 ± 0.005	Wisotzki et al. (1993); Lehar et al. (2000)
CLASS B1127+385	-		0.80 ± 0.07				-1.39 ± 0.08		Koopmans et al. (1999)
CLASS B1152+199		x	0.3304 ± 0.0012	0.0225 ± 0.0006	0.439	1.019	-1.8058 ± 0.0008	-1.9885 ± 0.0003	Toft, Hjorth, & Burud (2000); Rusin et al. (2002)
SDSS1155+6346				0.48 ± 0.06	0.176	2.89		-1.70 ± 0.05	Pindor et al. (2004)
SDSS1206+4332		x		0.637 ± 0.008		1.79		-1.568 ± 0.007	Oguri et al. (2005)
Q1208+101	-			0.229 ± 0.007		3.80		-1.871 ± 0.004	Magain et al. (1992); Lehar et al. (2000)
SDSS1226-0006	-								Oguri et al. (2004); Eigenbrod et al. (2006)
SDSS1335+0118				0.346 ± 0.002				-1.7954 ± 0.0014	Oguri et al. (2004)
Q1355-2257				0.1934 ± 0.0005		2.00		-1.8925 ± 0.0003	Morgan et al. (2003)
HST14164+5215	-								Ratnatunga, Griffiths & Ostrander (1999)
CLASS B1600+434			0.80 ± 0.03	0.77 ± 0.05	0.41	1.59	-1.39 ± 0.03	-1.43 ± 0.05	Jackson, Xanthopoulos & Browne (2000)
PMNJ1632-0033			0.0765 ± 0.0013	0.031 ± 0.003		3.424	-1.9597 ± 0.0007	-1.984 ± 0.002	Winn et al. (2002)
FBQ1633+3134				0.297 ± 0.003		1.52		-1.828 ± 0.002	Morgan et al. (2001)
SDSS1650+4251				0.144 ± 0.010		1.54		-1.922 ± 0.006	Morgan, Snyder & Reens (2003)
PKS1830-211		x	0.743 ± 0.005	0.0156 ± 0.0015	0.89	2.51	-1.464 ± 0.005	-1.9921 ± 0.0008	Subrahmanyam et al. (1990); Lehar et al. (2000)
PMNJ1838-3427			0.0697 ± 0.0015	0.038 ± 0.006		2.78	-1.9634 ± 0.0008	-1.981 ± 0.003	Winn et al. (2000)
PMNJ2004-1349		x	0.98 ± 0.03	0.89 ± 0.08			-1.10 ± 0.07	-1.25 ± 0.14	Winn et al. (2001)
MG2016+112		x	1.06 ± 0.05	0.75 ± 0.02	1.01	3.27		-1.45 ± 0.02	Schneider et al. (1985)
B2108+213		x	0.47 ± 0.02	0.39 ± 0.05			-1.71 ± 0.02	-1.76 ± 0.03	McKean et al. (2005)
CLASS B2319+051	-		0.1979 ± 0.0013		0.62		-1.8899 ± 0.0008		Rusin et al. (2001)

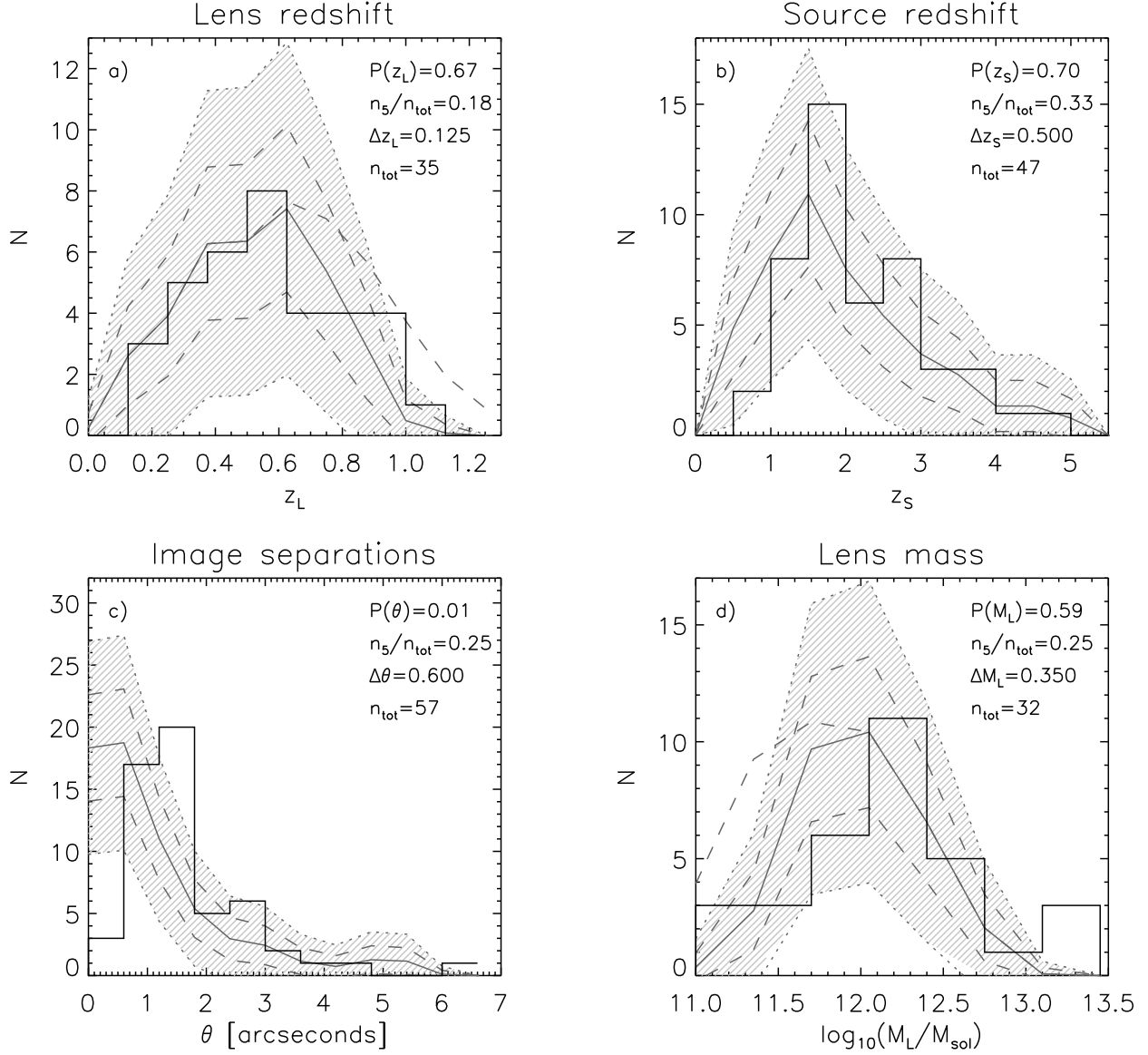


Figure 4. Lens data generated by the simplest model in our Monte Carlo code. Panel a) presents distribution of the lens redshifts. The sampled redshift distribution contains some lenses with redshifts $z_L > 1$ (dashed line), but they vanish if the lens object magnitudes are accounted for (solid line). Shaded region outlines 2σ -region corresponding the Poisson noise proportional to the observed lens sample size. Over-plotted histogram describes redshift distribution of observed lenses. Panel b) shows similar redshift distribution for the sources. The image separations in arcseconds (θ) are presented in panel c) and sampled lens masses compared to the lens masses inferred from observed magnitudes for the lens objects are plotted in panel d). Note, that here the symbol θ for the image separation should not be confused with the image coordinate ratio in equation (13). The observed data is from the CASTLES survey catalogue. Each panel lists a Kolmogorov – Smirnov test probability P against observed data, ratio of the bins with more than five data points (n_5) to the total number of data points (n_{tot}), binsizes (Δz_L , Δz_S , $\Delta\theta$, ΔM_L), and total number of lens systems (n_{tot}).

In figure 4, the panel c) presenting image separation distribution has low Kolmogorov – Smirnov probability. Note, that here θ is image separation in arcseconds, that should not be confused with the image coordinate ratio in equation 13. The mock data distribution follows the observed image separations when $\theta \gtrsim 1''$, while lenses with tighter image separations are over represented. We believe that this discrepancy is a result from an observational bias. Because the observed lens systems are not from a single systematic survey, the lenses with small image separations are under-

represented in observations (lenses with image separation $\gtrsim 1''$ are easier to detect). It is clear, that the lens data acquired with a large array of different instruments is far from being statistically uniform. Therefore, chosen values for the magnitude limit and image separation limit were determined from fitting to the data.

Although we conducted a parameter sweep for magnitude limit M_{lim} , image separation limit θ_{lim} and parameters U , P , f_E , it should be emphasized that we do not try to find the best fit for the base-distribution parameters.

Table 2. Numerical values for the parameters used by our Monte Carlo code. The upper part of the table lists parameters for the Faber-Jackson relation and redshift evolution in the differential optical depth for lensing $d\tau/dz(M_L, z_s)$. The lower part contains parameters for the quasar luminosity function $\Phi(L, z_s)$. See text for the quoted references on the further details about the parameters.

parameter	Spiral	S0	Elliptical
$\frac{d\tau}{dz}$			
α	-1.16	-0.54	-0.54
$n_*(h^3\text{Mpc}^{-3})$	1.46×10^{-2}	0.61×10^{-2}	0.39×10^{-2}
γ	2.6	4.0	4.0
$\sigma_*(\text{km s}^{-1})$	144	206	225
U	-0.20	-0.20	-0.20
P	1.20	1.20	1.20
f_E	0.95	0.95	0.95
parameter	$(z_s > 3)$	$(z_s < 3)$	
Φ			
β_h	2.58	3.43	
β_l	1.64	1.64	
$\Phi_*(\text{Gpc}^{-1})$	624	624	
$L_{*,0}(L_\odot)$	1.50×10^{11}	1.50×10^{11}	
z_*	1.60	1.60	
ζ	2.65	2.65	
ξ	3.30	3.30	

We use these values only for providing as realistic test data for the CSL-analysis method as possible. It should also be noted that even though the generated data is not exactly fitting the observed sample, it should contain similar internal correlations as the real data. Therefore it can provide decent test cases for our method. We use bolometric magnitude limit is $M_{\text{lim}} = 30.5$ mag and image separation limit $\theta_{\text{lim}} = 0.2''$. Table 2 summarizes chosen parameters for the base distributions. For further explanation about physical meaning of the parameters, see Ofek, Rix & Maoz (2003) and Wyithe & Loeb (2002).

In the following subsections, we explore the effects from the ellipticity of the lensing potential, the substructure within the lensing halo, and the source variability coupled to the time-delay that can distort the magnification ratios from the lensing events. This is done by creating mock lens catalogues with different degrees of perturbations and performing the CSL-analysis on them.

4.1 The Basic Concept

The concept of the CSL value is to disentangle cosmology and geometrical configuration of the each lens event from the properties of the lens halo profile. These factors cancel out in the derivation of the CSL equations (14) and (15). However, they do have an indirect influence on the underlying sample of the lens systems and can affect the statistics of the CSL values.

The disentanglement of the lens halo properties from the other factors in the CSL analysis is possible because we assume simple lensing properties – the lens potential is axially symmetric and the source images are uniformly distributed on the strong lensing region of the source plane. If there is a strong bias in the actual source image locations on the source plane, it can distort the resulting CSL distribu-

tion. Such a bias can emerge in a magnitude limited sample, where sources at the high magnification region of the source plane are over-represented in the total sample.

We have constructed a numerical probability function for the CSL values (α_{CSL}) with an universal cusp slope α (see appendix 2.2). We fit this function to a histogram of α_{CSL} values calculated from the (mock) data. In the fitting procedure, we use the Levenberg-Marquardt method and standard χ^2 -statistics. The fitted parameters are the universal cusp slope value α and normalization parameter n . Figure 5 illustrates such a fit.

The universal density profile has been one of the main assumptions in studying the properties of dark matter haloes. A population of lenses with a single cusp slope parameter α produces a distinctive CSL-value distribution (figure 5) that is very different from completely random profiles. Figure 6 shows CSL distribution of a lens population with uniformly distributed random profiles with α in range $[-2, -1]$ (hatched area), and second lens sample with profile slope parameters in same range with normal distribution (expectation value $\langle\alpha\rangle = -1.5$ and $\sigma_\alpha = 0.15$, solid line).

When performing fits on binned data, there are some issues to be considered, see e.g. Humphrey, Liu & Buote (2009). We tested several goodness-of-fit functions and bin-sizes in order to find such a configuration that can recover the universal cusp slope value from the data as often as possible. We have chosen to use the previously mentioned goodness-of-fit function and bin the data in 14 bins in range $\alpha_{\text{CSL}} = [-2.0, -1.07]$. By using our binning selection and goodness-of-fit function, we were able to recover the universal cusp slope α with 2σ accuracy in most of the cases (cusp slope value $\alpha = [-2.0, -1.1]$ and catalogue size $N_{\text{lens}} = [30, 100]$).

The quoted error limits for the fitted parameters and corresponding rejection probabilities are calculated with the Monte-Carlo method. We use a bootstrap method to create hundred data sets that are fitted using the same procedure as the original data. These fits are employed for error estimates and rejection probability calculation. This is a well known procedure that has been employed by several authors, see e.g. papers by Buote et al. (2003) and Humphrey et al. (2006) for further information.

There are certainly more suitable values for binning that can be adapted for certain sizes of samples and values for the universal cusp slope α . However, we emphasize a good overall performance with wide range of sizes for the lens samples and parameters. If not mentioned otherwise, we use these choices in the analysis presented in the following subsections.

4.2 Lens Ellipticities

The CSL-analysis is based on an axially symmetric lens model. In reality, the observations and the N-body simulations indicate that the dark matter haloes are triaxial ellipsoids, see e.g. Hayashi, Navarro & Springel (2007) and references therein. Here we examine the effects from asymmetries that can distort the CSL-analysis results by changing the observed magnification ratios.

We have generalized our axially symmetric lens model to the elliptic lens potential case. The isopotential surfaces of the elliptic lens follow similar surface density as the ax-

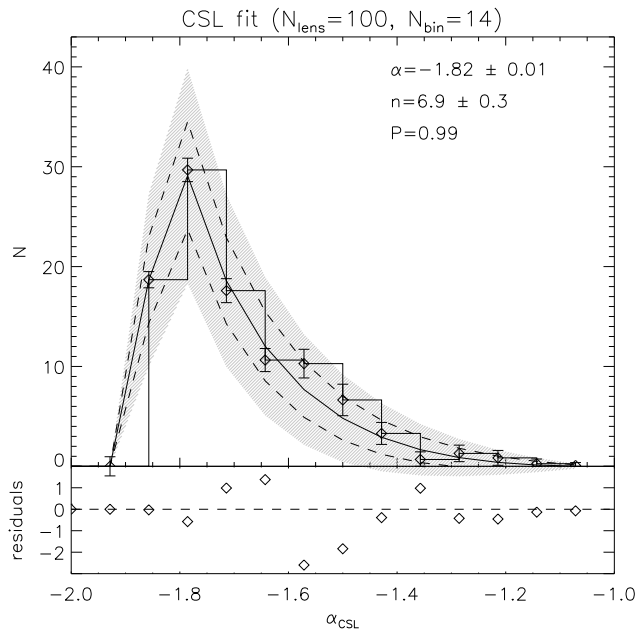


Figure 5. Fit of a re-normalized theoretical probability function for the CSL distribution of a lens population with cusp slope $\alpha = -1.8$. Jagged histogram and corresponding diamond symbols with error bars present histogram data for α_{CSL} values calculated from the mock sample. Error bars correspond to 0.1 magnitude absolute error in photometry. Thick solid curve represents fitted CSL-distribution, with σ (dashed line) and 2σ (shaded region) outlining the Poisson shot noise error region. The fitted cusp slope value for the data is $\alpha = -1.82 \pm 0.01$ and $n = 6.9 \pm 0.3$ with $P < 0.01$ rejection probability.

ially symmetric lens model, equation (1). Our elliptic lens model approaches the axial model with eccentricity value $e \rightarrow 0$. The lens equations were derived from numerical integrals for elliptic lensing presented in Schramm (1990) and Schneider, Ehlers & Falco (1992).

The elliptic lenses can produce four image lenses, when the source image is located inside the inner diamond shaped caustic curve. This configuration is related to the Einstein ring in the case of axial symmetry. Our Monte Carlo code accepts only double image lens systems into the sample, i.e. all the source images must be outside the inner caustic. The size of the area at the source plane demarcated by the inner caustic curve depends on the cusp slope α of the profile and on the eccentricity e of the halo. In general, a larger inner caustic area means stronger deviations from the axially symmetric lensing.

Strongly cusped lens profiles can tolerate high degrees of eccentricities without significant difference in the image flux ratio to the axially symmetric case. Deviations from the axially symmetric model grow progressively larger with shallower profiles and increasing eccentricities. This trend is illustrated by figure 7, in which we have examined an unrealistic scenario where all the lenses have constant eccentricity. We have constructed lens catalogues with cusp slope values $\alpha = [-1.9, -1.75, -1.6, -1.45, -1.3]$ and varied eccentricity of the lensing potential. We investigated eccentricities in range $e = [0, 0.6]$ with 0.05 increments.

In figure 7, each cusp slope value is represented with

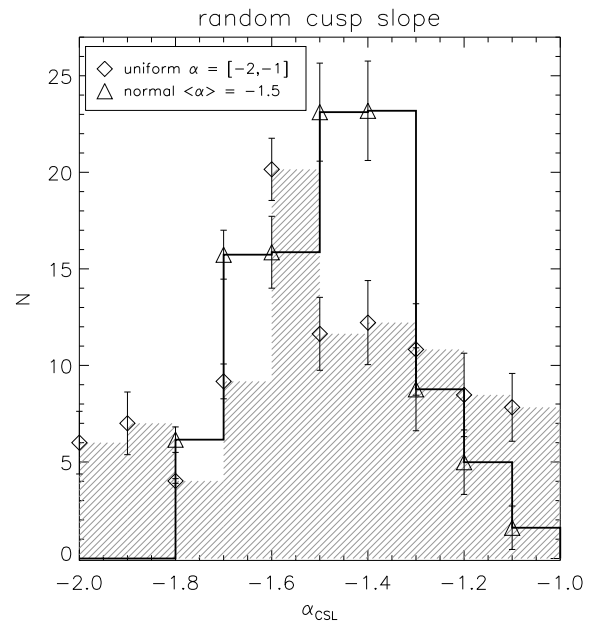


Figure 6. If the cusp slopes of lensing haloes are random, characteristic CSL-distribution (see figure 5) disappears. This figure illustrates how a population of lenses with random cusp slope values appears in the CSL histogram. The hatched area is a histogram of a lens population with cusp slope values that have uniform distribution. Thick line presents histogram of a lenses with normal cusp slope values with an expectation value at $\langle \alpha \rangle = -1.5$, and variance $\sigma_\alpha = 0.15$. Error bars represent 0.1 magnitude absolute error in photometry.

a horizontal dashed line. Plotted data points correspond to fits to mock catalogues including error estimates with each value of eccentricity. Data points are plotted until the ellipticity makes the CSL distribution unrecognisable (cutoff vanishes and tail becomes erratic). The figure clearly shows the aforementioned trend for cusped profiles; the fit tends to increasingly overestimate the cuspsiness of the profile with increasing halo ellipticity. The cutoff comes earlier with shallower profiles.

We model the lens potential eccentricities with log-normal random distribution with expectation value $\langle e \rangle$ and variance σ_e . As a reference case, we follow the treatment by Huterer, Keeton & Ma (2005) and adopt the distribution of ellipticities measured for 379 early-type galaxies by Jørgensen, Franx & Kjaergaard (1995). The distribution has mean $\langle e \rangle = 0.31$ and $\sigma_e = 0.18$, with upper limit $e < 0.6$.

Our results indicate that, regardless of realistically elliptical lens haloes, the modelled CSL value distribution can recover the universal cusp slope up to slope value $\alpha \sim -1.7$ and give a rough guess for the exact value up to $\alpha \sim -1.5$ that is always an overestimate. See figure 8.

4.3 Substructure

The dark matter haloes should have several sub-haloes that generate irregularities in the lensing potential. These irregularities can corrupt the macro-lens magnification ratio and distort the CSL-distribution. Here we have chosen to follow similar approach as in Rozo et al. (2006). We model the ef-

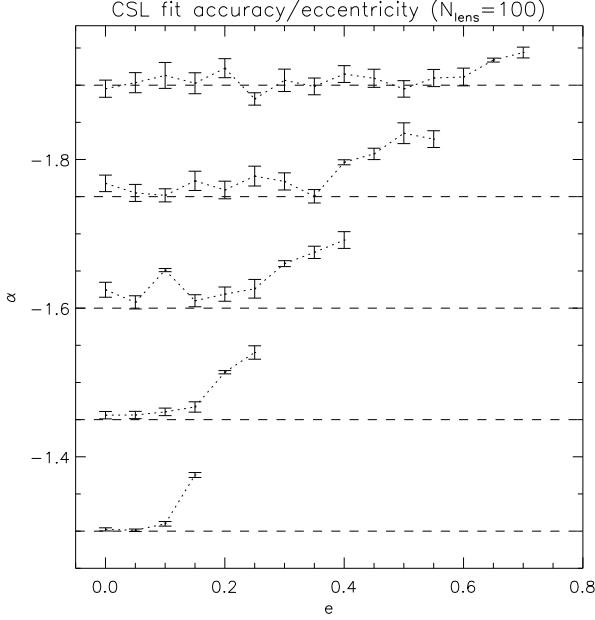


Figure 7. We have compiled lens catalogues with cusp slope values $\alpha = [-1.9, -1.75, -1.6, -1.45, -1.3]$ with constant eccentricities. The lens catalogues have 100 lens systems. The x-axis measures eccentricity e and the y-axis cusp slope α . Each data point corresponds to a fitted CSL distribution with error estimates. All the fits with recognisable cutoff in the CSL value distribution are plotted. If the eccentricity is further increased, characteristic shape (figure 5) of the distribution vanishes.

fects from the substructure on the magnification of images with N linearized perturbers contributing with $\delta\mu_i$ to the total perturbation δ . When contribution from all the perturbers is added together, we get the total perturbation

$$\delta = \frac{\sum_i^N \delta\mu_i}{|\mu|} = 2|\mu| \left[(1 - \kappa) \sum_i^N \delta\kappa_i - \gamma \sum_i^N \delta\gamma_i \cos(2\phi_i) \right], \quad (32)$$

where κ and γ are macro-lens convergence and shear, whereas $|\mu|$ is macro-lens magnification. Each perturber is located at radial coordinates θ_i and ϕ_i , and convergence perturbations $\delta\kappa_i$ and shear perturbations $\delta\gamma_i$ are corresponding contributions from the i th perturber. It is assumed that $|\delta\mu_i| \ll 1$, thus the astrometric perturbations by the substructure are negligible and only the changes in the image fluxes are considered.

We follow the analysis by Dalal & Kochanek (2002) and Rozo et al. (2006) by employing a pseudo-Jaffe density profile

$$\rho(r) \propto r^{-2}(r^2 + a^2)^{-1} \quad (33)$$

for individual perturbers. Here r is radial coordinate and a is an effective tidal radius. As presented in Rozo et al. (2006), we parametrize the tidal radius with λ_a as

$$a = \frac{\pi\lambda_a\sqrt{bb_H}}{2}, \quad (34)$$

where b is the Einstein radius of the perturber and b_H the corresponding radius for the macro-lens model. Convergence and shear contribution ($\delta\kappa_i$ and $\delta\gamma_i$) from the i th perturber at polar coordinates ($\theta_i = k_i x_e r_s / D_L, \phi_i$) is

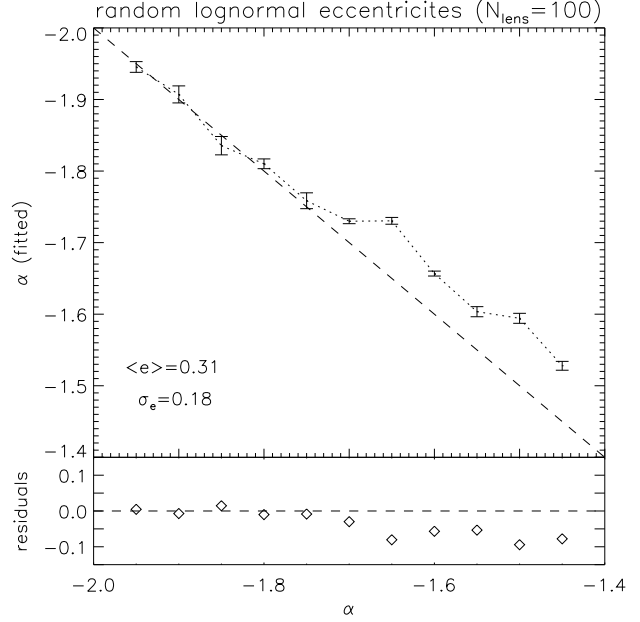


Figure 8. Cusp slopes from the fitted CSL values using lognormal random distribution for the lens halo eccentricities (see text). The x-axis has the cusp slope value used in the mock catalogue generator, and the y-axis has fitted cusp slope value. Diagonal dashed line marks the exact fit. Each data point denotes a result from a CSL distribution fit to a compiled lens catalogue, with error estimates. Lower panes shows fit residuals. Fit gets progressively worse with more shallow profile until at $\alpha \sim -1.45$ the characteristic shape of the CSL value distribution is too distorted in order to make a sensible fit to the data.

$$\delta\kappa_i = \tilde{b} \left(\frac{1}{2\theta_i} - \frac{1}{2\xi} \right) \quad (35)$$

and

$$\delta\gamma_i = \tilde{b} \left[\frac{1}{2\theta_i} + \frac{1}{2\xi} - \frac{a}{\theta_i^2} \left(\frac{\xi}{a} - 1 \right) \right]. \quad (36)$$

The mass of the perturber is $m = \pi a \tilde{\Sigma}_{cr} D_L^2$, while \tilde{b} is defined by

$$\frac{b}{\tilde{b}} = 1 + \frac{a}{b} - \left[1 + \left(\frac{a}{b} \right)^2 \right] \quad (37)$$

and ξ is

$$\xi \equiv \sqrt{\theta_i^2 + a^2}. \quad (38)$$

When $a \rightarrow \infty$ the pseudo-Jaffe lens profile approaches SIS profile, and when $a \rightarrow 0$ the profile corresponds to a point mass lens.

Mass spectrum s of the perturbers is assumed to follow $ds/dm \propto m^\beta$, where we choose $\beta = -1.8$ as in Gao et al. (2004). The amount of substructure is defined by a ratio of the substructure surface density to the critical density $f_{sub} = 2\Sigma_s/\Sigma_{cr}$. The mass spectrum is parametrized also by the cutoff at the substructure mass value m_{max} that is chosen to be 1 per cent of the mass within the Einstein radius (mass M_E) of the lens object.

We account the substructure perturbations to the image magnification in the synthetic lens catalogue generation as follows: the magnification change of the each image is es-

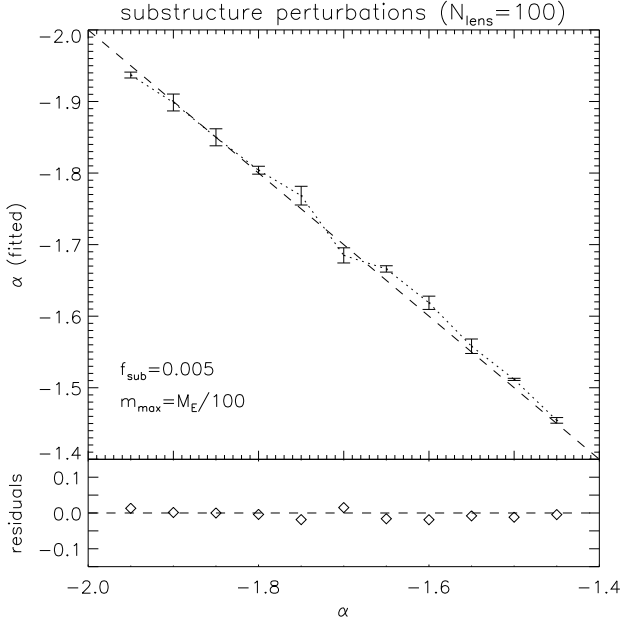


Figure 9. Cusp slopes from the fitted CSL values including substructure perturbations to then magnification. The x-axis has the cusp slope value used in the mock catalogue generator, and y-axis has fitted cups slope value. Diagonal dashed line marks the exact fit. Each data point denotes a result from a CSL distribution fit to a compiled lens catalogue, with error estimates. Lower panes shows fit residuals.

timated by randomly generating 1000 perturbers uniformly distributed at the lens surface with a surface density that is determined by the f_{sub} . The total perturbation δ_{tot} is then estimated from the equation (32) with negative surface mass component in order to guarantee the mass conservation

$$\delta_{\text{tot}} = \delta - |\mu|(1 - \kappa)f_{\text{sub}}. \quad (39)$$

The perturber masses follow the previously discussed power law mass spectrum with index β . The total perturbation δ_{tot} is then added to the total magnification of the image, corresponding to the macro lens shear and convergence.

Again, we follow the Rozo et al. (2006) with the parametrization of the substructure and choose tidal radius parameter $\lambda_a = 4.0$, and substructure surface density $f_{\text{sub}} = 0.005$.

We study the goodness of the CSL fit as a function of the universal cusp slope of the generated lens catalogue with constant strength for the substructure. The lens catalogues are generated with an axially symmetric lens model with cusp slopes α ranging in $[-1.95, -1.45]$. The results are summarized in figure 9. All the fits are very close to the original value, although it would seem that fits get slightly worse at higher values for the cusp slope ($\alpha \gtrsim -1.7$).

Although the substructure can significantly alter the observed flux ratio of the images, this can happen only at the vicinity of the critical curves for lensing (at the source coordinate $l \sim 0$ or $l \sim l_{\text{max}}$). These kinds of lens systems produce either strongly magnified Einstein rings or triple image lenses that are excluded from the analysis by the selection criteria. Furthermore, because such lens systems have incidence probability proportional to the square of the ratio

l/l_{max} , they should be comparatively rare when the source images are uniformly distributed at the source plane.

Here it should be noted, that a similar treatment could be applied for micro-lensing. However, because the CSL-limit analysis is based on double image lenses where the images are generally not close to the critical curves, we assume that the effects from micro-lensing can be safely neglected.

4.4 Time-delay

In the double image lenses, the lensed images represent the source at different moments in time in the rest frame of the source. This is a consequence of a different light propagation distance for each image (geometric time-delay) and different gravitational potential along the light ray trajectory (potential time delay). As a consequence, the observed flux ratio is different from the magnification ratio of the images if the source flux is varying at suitable timescale. This can distort the acquired CSL-distribution.

We calculate the time delay from the lensing potential generated by our parametrized density profile. For definitions of time delay, see for example Schneider, Ehlers & Falco (1992). The source variability is modelled by generation power law noise, that is parameterized according to the observational relations published in Vanden Berk et al. (2004).

Source flux variations are modelled by generating power law variations Δm around the baseline magnitude of the source sampled from the quasar luminosity function. The power spectrum of the magnitude variations is

$$\Phi = \Phi_0 \omega^{-\eta}, \quad (40)$$

where ω is frequency, η power law index and Φ_0 corresponding normalization. On generating power law noise, see paper by Timmer & König (1995).

Noise with characteristics defined by (40) have variance

$$\sigma_{\Delta m}^2 = 2 \int_{2\pi f}^{\infty} d\omega \Phi(\omega) = \frac{2\Phi_0(2\pi)^{-\eta}}{\eta - 1} f^{1-\eta}, \quad (41)$$

where f is the minimum frequency to be considered. Corresponding covariance function for the magnitude $m = m(\tau)$ is

$$\begin{aligned} B(\Delta\tau) &= \langle m(\tau)m(\tau + \Delta\tau) \rangle = \langle \Delta m^2 \rangle \\ &= \int_{2\pi f}^{\infty} d\omega \cos(\omega\tau) \Phi(\omega) = \frac{1}{2} \Phi_0 \tau^{\eta-1} A(\eta, f), \end{aligned} \quad (42)$$

that is written at time τ with time lag $\Delta\tau$. In previous equation we define $A(\eta, f)$ as

$$A(\eta, f) = e^{-i\pi(1-\eta)/2} \Gamma(1 - \eta, i2\pi f) + e^{i\pi(1-\eta)/2} \Gamma(1 - \eta, -i2\pi f), \quad (43)$$

where $\Gamma(x, y)$ is the incomplete gamma-function. The variability function $V = V(\tau)$ and model for it are defined as

$$V(\tau) = \sqrt{\frac{\pi}{2} \langle \Delta m \rangle^2 - \langle \sigma_{s/n}^2 \rangle} = V_0 \left(\frac{\tau}{\tau_0} \right)^{\gamma}, \quad (44)$$

where V_0 and τ_0 , that are determined from the observations, parametrize the model. Here $\langle \sigma_{s/n}^2 \rangle$ is the signal to noise ratio of the variations.

When $\langle \Delta m^2 \rangle \sim \pi \langle \Delta m \rangle^2 / 2$, we get from the definition of the variance and equations (41) and (42) the relation between power spectrum parameters and the variability function. The power law indices are related as

$$\eta = 1 + 2\gamma \quad (45)$$

and normalization as

$$\Phi_0 = \frac{4V_0}{\pi A(\eta, f) \tau_0^{2\gamma}}. \quad (46)$$

Here it should also hold $\langle \sigma_{s/n}^2 \rangle = \pi |\sigma_{\Delta m}^2|$.

The normalization Φ_0 and the power law index η characterizing the power law noise are calculated from the variability function presented by Vanden Berk et al. (2004), where they study photometric variability of roughly 25 000 quasars in the SDSS survey.

In their paper, they estimate the variability function power law index as $\gamma = 0.246 \pm 0.008$ and characteristic time scale $\tau_0 = (5.36 \pm 1.46) \times 10^5$ d. The normalization of the variability function (44) is parametrized as

$$V_0 = v(M)v(\lambda_R)v(z) \quad (47)$$

with the absolute magnitude of the quasar M , observed rest-frame wavelength λ_R and redshift of the quasar z . Here we set

$$v(M) = 10^{\beta M/2.5} \quad (48)$$

in which $\beta = 0.246 \pm 0.005$. Correspondingly

$$v(\lambda_R) = a_0 e^{-\lambda/\lambda_0} + a_1 \quad (49)$$

with $a_0 = 0.616 \pm 0.056$, $a_1 = 0.164 \pm 0.003$ and $\lambda_0 = 988 \pm 60 \text{ \AA}$. And finally

$$v(z) = (0.019 \pm 0.002)z + (0.037 \pm 0.005). \quad (50)$$

The time lag $\Delta\tau$ is acquired from the time delay equations, and we choose rest-frame wavelength corresponding to the observed B -band wavelength. The absolute magnitude is acquired from the sampled luminosity of the quasar.

We convert the parametrized variability function to the power law noise index η and corresponding normalization Φ_0 , and obtain random change in the flux of the source by generating similar power law noise. This changed flux (that equals the baseline flux sampled from the quasar luminosity function with the random change for the each image) is then correspondingly magnified by the lens and inserted into the standard mock lens catalogue generator.

We study the effects from the time delay coupled to the source variability by generating several mock catalogues with an universal cusp slope values α ranging in $[-1.95, -1.45]$. The mock catalogues are generated with an axially symmetric model. The fitted CSL values are presented in figure 10.

Inclusion of the source variability seems to slightly strengthen the acquired cusp from the lensing data. Although all the fits are reasonably good, strongly cusped catalogues are most affected by the source variability.

4.5 Combined error sources

In the previous subsections, we have examined the strength of several distortions on the CSL statistics with the simplest

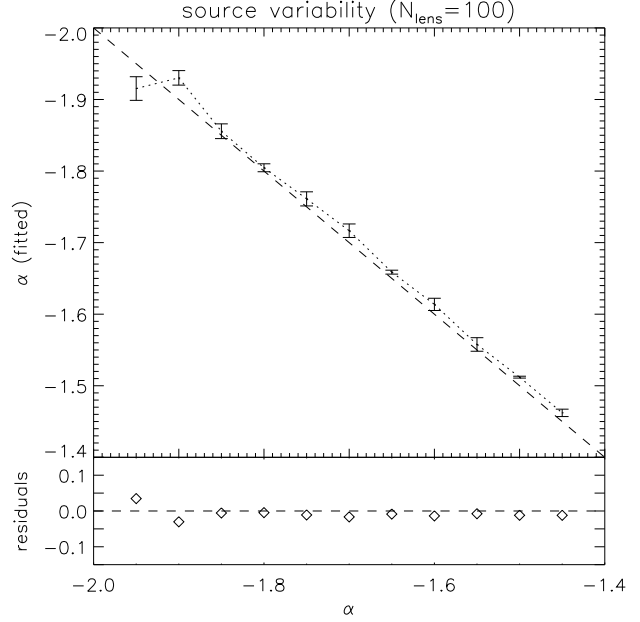


Figure 10. Cusp slopes from the fitted CSL values including source variability induced time delay perturbations to the image flux. The x-axis has the cusp slope value used in the mock catalogue generator, and y-axis has fitted cusp slope value. Diagonal dashed line marks the exact fit. Each data point denotes a result from a CSL distribution fit to a compiled lens catalogue, including error estimates. Lower panel shows fit residuals.

possible model. Here we add all the contributing factors (ellipticities, halo substructure and time-delay) together in order to see what is the applicability of our method.

We study the goodness of the CSL fit as a function of the universal cusp slope value in the mock catalogues. We use elliptical lens model with random log-normal eccentricities as in subsection 4.2. The modelled lens systems possess similarly parametrized substructure as in 4.3 and source variability corresponding to the previous subsection 4.4.

The results of the fits are presented in figure 11. It would seem that a simple axially symmetric model with an assumption of uniform source image distribution at the source plane can capture essential properties of the double image lenses in the presence of higher order effects when calculating the CSL statistics.

In general, the CSL goodness-of-fit χ^2 -surface contains a local minimum inside each bin. In the fits that are presented here, we have always chosen the global minimum. However, in some cases there are two local minima that have almost the same χ^2 values resulting two equally good fits in statistical sense. Such problems can be resolved by manually adjusting the binning to cover the range of α_{CSL} values in an optimal way. We have chosen to use a fixed binning that produces fits that should become progressively poorer when the universal cusp slope approaches $\alpha = -1$ because the data is assigned to fewer bins correspondingly. However, the leftover zero bins are fitted into the model with estimated error bars, thus the recovered error bars for α do not change significantly. This is a conscious choice that was made in order to study the error sources as a function of the cusp

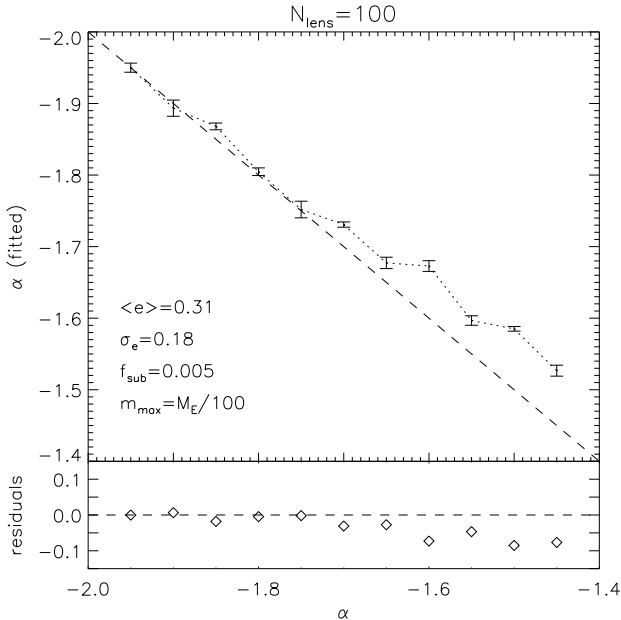


Figure 11. Cusp slopes from the fitted CSL values with all the examined perturbation sources (lens ellipticity, substructure and time delay effects coupled to the source variability). The x-axis has the cusp slope value used in the mock catalogue generator, and y-axis has fitted cusp slope value. Diagonal dashed line marks the exact fit. Each data point denotes a result from a CSL distribution fit to a compiled lens catalogue, including error estimates. Lower panel shows fit residuals.

slope in a consistent way. In principle, an adaptive binning should produce better results, but as the real data is spread over rather wide range of the α_{CSL} values, we hold to our previously adopted binning scheme.

5 FITTED CSL STATISTICS

In this section, we apply the statistical analysis of the CSL values to the real double image lens data. We use our double image lens sample described in section 3 to study the distribution of the CSL values. The calculated CSL values for each lens system are presented in the table 1. These values are fitted to the theoretical distribution (see appendix 2.2). The fit produces estimates for an universal cusp slope value α and corresponding normalization n proportional to the size of the sample.

In the fitting procedure, the error limits for the histogram were created using the Monte-Carlo method. Thousand distributions were constructed with simulated Gaussian errors according to the measurement errors in the flux ratios. The data points in the presented histogram are mean values, and the corresponding error limits are the standard deviation calculated from these constructed histograms. In some cases values at the end points of the distribution had zero error limits. Those were estimated upwards with mean of non zero errors within the distribution. We use the same setup for the data as for the Monte Carlo testing described in the previous section. The details are presented in section 4.1.

5.1 Single population model

We start our analysis with an assumption of a single universal halo profile. The acquired cusp slope value for this lens population is $\alpha = -1.95 \pm 0.02$. The value of the normalization parameter is not interesting, because it is simply scaling the probability function to the size of the sample. The resulting fit is presented in figure 12. The acquired value for the cusp is close to the value of an isothermal sphere (SIS).

All the data points below $\alpha_{\text{CSL}} \sim -1.5$ fall well into the one Poisson- σ range of the model. However, at $\alpha_{\text{CSL}} > -1.5$ there are two data points well outside of the 2σ -Poisson noise range. These data points represent roughly 18 per cent of the total sample of lens systems. All corresponding lens systems cannot belong to the same profile group as the acquired fit because perturbations have a tendency to steepen the acquired cusp slope. One explanation could be that these are strongly sheared systems, but there are several arguments against this possibility.

The fact that the deviating lens systems are rather tightly clustered around value $\alpha \sim -1.5$ does not support sheared lens scenario. Randomly sheared systems should produce wider distribution, with similar characteristics as random cusp slope values (see figure 6). Strongly cusped haloes are also more resistant against the deviations from the axial symmetry than the haloes with shallower cusps (see section 4.2). Additionally, sheared systems that have strongly deviating magnification ratio from the axially symmetric value, very often produce more than two images in similar fashion as strongly elliptic haloes. Such lens systems are excluded from the analysis by the selection criteria used to construct our lens sample.

A single universal cusp slope value cannot fully explain the observed CSL-value distribution. Therefore, we investigate also a possibility that this deviation is a signature of a second population of haloes with their own characteristic density profile.

5.2 Dual population model

The dual population model (populations are abbreviated as H1 and H2) is implemented by adding two individually normalized distributions together, producing a model with four parameters. This model is fitted to the observational data in a similar fashion as the single population model in the previous subsection. The fit produces estimates for the universal cusp slope values α_{H1} and α_{H2} for both populations, and the corresponding normalization values n_{H1} and n_{H2} .

The detailed fit to this data is presented in figure 13. The acquired values are cusp slope $\alpha_{\text{H1}} = -1.95 \pm 0.02$ and normalization $n_{\text{H1}} = 2.5 \pm 0.7$ for the population H1 and for the population H2 correspondingly $\alpha_{\text{H2}} = -1.49 \pm 0.09$, $n_{\text{H2}} = 0.5 \pm 0.3$. Normalization values n_{H1} and n_{H2} gives the relative abundance of population H1 and population H2 lens objects in the sample. Our results indicate that 83 per cent of the lens objects belong to the population H1 and 17 per cent to the population H2 with 4 per cent error margins in both values. This suggests that on average roughly one sixth of the lens objects capable of strong lensing belong to the second population with shallower cusp slope.

The dual population fit is better than the single population fit, which is to be expected because number of free

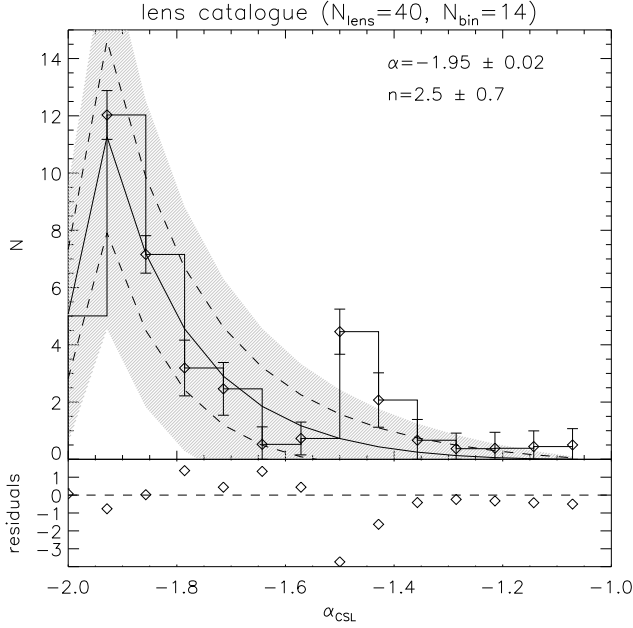


Figure 12. A single population fit of a re-normalized theoretical probability function for the CSL value distribution from an observational lens catalogue. Jagged histogram and corresponding diamond symbols with error bars present histogram data for α_{CSL} values calculated from the data. Error bars correspond to measurement errors in photometry. Thick solid curve represents fitted CSL-distribution, with σ (dashed line) and 2σ (shaded region) outlining the Poisson shot noise error region. The fitted cusp slope value for the data is $\alpha = -1.95 \pm 0.02$ and normalization $n = 2.5 \pm 0.7$.

parameters is doubled. In practice all the data points are now inside the one- σ Poisson noise range of the model. Population I parameters are the same as in the single population model. However, the second population parameters have much larger relative error range than population H1 parameters, indicating large uncertainty. This reflects the small size of the lens sample. Additionally, the second population cusp slope has such a value that is much more affected by the perturbations than the cusp slope value for population H1 lenses.

5.3 Is the second population real?

Regardless of the Poisson noise limits, we are very concerned if the observed feature at $\alpha_{\text{CSL}} \sim -1.5$ is nonetheless noise induced. The statistical fit with such a small sample compared to the number of fitted parameters should be regarded with high suspicion. Additionally, the signature of the second population is relatively weak when considering the error limits for the fitted parameters of the second population.

Therefore, we set up a Monte-Carlo experiment in order to find out the probability that the second population hypothesis could be rejected. We generated 100 lens catalogues with 40 lens systems by randomly sampling a mock catalogue of 4000 lens systems. The mock catalogue was created using a single lens population with a cusp slope value of $\alpha = -1.95$ and accounting for the lens ellipticities, the sub-structure and the source variability. These generated cata-

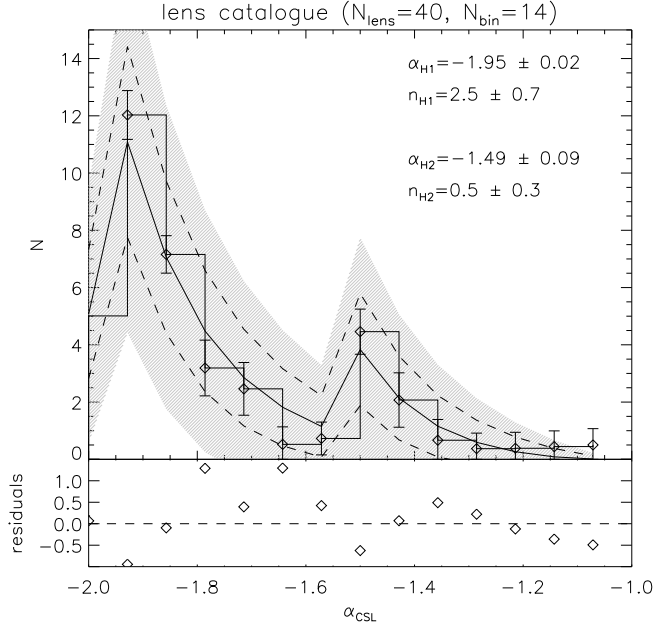


Figure 13. A dual population fit of a re-normalized theoretical probability function for the CSL value distribution from an observational lens catalogue. Jagged histogram and corresponding diamond symbols with error bars present histogram data for α_{CSL} values calculated from the data. Error bars correspond to measurement errors in photometry. Thick solid curve represents fitted CSL-distribution, with σ (dashed line) and 2σ (shaded region) outlining the Poisson shot noise error region. The fitted cusp slope value for the data is $\alpha_{\text{H1}} = -1.95 \pm 0.02$ and normalization $n_{\text{H1}} = 2.5 \pm 0.7$ for the first population. The second population has corresponding determined values $\alpha_{\text{H2}} = -1.49 \pm 0.09$ and $n_{\text{H2}} = 0.5 \pm 0.3$.

logues were fitted with a single population model. The probability to reject the second population hypothesis is equal to the probability to get as strong signature of the second population as in the observed lens catalogue.

In the observations, the second population feature exceeds the 2σ noise limit by factor 1.8 at α_{CSL} range $[-1.6, -1.4]$. In order to interpret the noise induced feature as the second population, we set a condition that the dataset must contain a data point that exceeds the 2σ level by similar factor at the same range. We found one such catalogue out of one hundred, thus we estimate that the probability for rejection of the second population hypothesis is at order of one per cent.

On the other hand, the observational lens data contains two data points above the 2σ noise level. If we count lens samples that have two data points exceeding the 2σ threshold in α_{CSL} range $[-1.6, -1.4]$, we get a rejection probability of two per cent. If we add the factor of 1.8 excess condition, the probability goes down below one per cent.

Hence, we estimate that the rejection probability for the dual population hypothesis is roughly ~ 1 per cent.

6 DISCUSSION AND CONCLUSIONS

Our analysis is based on a geometric measure of a lens system - how much cuspieness does an axially symmetric lens

need in order to produce observed magnification ratio, i.e. the CSL value. In a sense, analogously to the curvature characterizing properties of space, it can be thought as a gauge characterizing localized properties of a lensing event. There is no need to define the exact global properties of the lensing potential in order to have a meaningful measure.

The CSL measure can be derived for axially symmetric lenses, and as a result, all the coefficients containing information on cosmology, cosmological angular separations of the lens and the source, lens mass and concentration are cancelled out. Only preserved quantities are the cusp slope and the image magnification ratio.

If we assume that the observed lenses have completely random orientations, thus neglecting effects from the magnification bias, a theoretical distribution of the CSL values can be calculated for a population of lenses. In that case, the properties of the lensing profile(s) determine the shape of the distribution. When we calculate the CSL value distributions from the real life data, we make an additional assumption that the observed image fluxes are determined only by the lens magnification of a constant flux source.

This chain of assumptions has its weak points, and we have tried to address most of them in section 4. Here we are going to do a brief summary of these, and discuss few unaddressed ones.

The first unaddressed issue is at the derivation of the magnification ratio equation (13). The equation is based on the inner part of the lens equation that does not behave correctly when the radial image coordinate at the lens plane exceeds the value k_B . Usually, this happens outside the strong lensing region, but if $\alpha \lesssim -2.0$ and the mass of the lens or the concentration is high enough, k_B can be located inside the strong lensing area ($k_B < k_{cr2}$).

This asymptotic behaviour of the lens equation was accounted for when the mock catalogues were created with the Monte Carlo method. The method works correctly with the mock data because the deviation from the correct value at $k \gtrsim k_B$ happens very slowly with the increasing radial image coordinate. Usually, difference becomes non-negligible only for images far into the weak lensing region even if k_B were inside the strong lensing area. Significant deviation requires unrealistically high mass or concentration for the halo.

The next issue is the error factors considered in section 4 – lens ellipticity, lens potential substructure, and source variability. Our earlier treatment was focused on examining the perturbations in the recovered cusp slope value. The analysis showed that the most severe disturbances originated from the lens ellipticities, although those were at manageable level when $\alpha < -1.4$ with random ellipticities.

The aforementioned factors have little or no effect because the analysis is restricted to the double image lenses by definition. At the double image region, deviations from the axially symmetric model are at their weakest. Differences become severe nearby the critical curves (at the origin $l \sim 0$ and at the border of the strong lensing region $l \sim l_{max}$), where the magnification diverges. Images nearby the critical curves produce either the Einstein rings ($l \sim 0$), quad lenses, or triple image lenses ($l \lesssim l_{max}$). Hence, the real life lensed images nearby critical curves are easily identified, and they can be excluded from the observational sample.

The similar reasoning can be used to counter arguments for effects from the sheared potential, micro-lensing, and the

magnification bias mentioned earlier. The bias cannot be very strongly present in the sample because the lens systems with excessive magnifications are excluded from the analysis.

Because the CSL analysis method is based on the flux ratios of the images, the extinction effects from intergalactic matter that affect both images in a similar way, can not change the results. In principle, considerable amount of differential extinction present at the lens object can corrupt the CSL value. However, the lensed images are very often well outside the visible lens object, which makes it improbable.

At this point we can conclude that the same reason that makes double image lenses unattractive targets for the substructure or the micro-lensing studies gives them ideal properties as a probe for the macro-lens profile. They are resilient against perturbations.

The main results from our study are the two halo profile populations. We get cusp slope value $\alpha_{H1} = -1.95 \pm 0.02$ and normalization $n_{H1} = 2.5 \pm 0.7$ for population H1 and for population H2 correspondingly $\alpha_{H2} = -1.49 \pm 0.09$, $n_{H2} = 0.5 \pm 0.3$. The normalization values indicate that 83 per cent of the lens objects belong to population H1 and 17 per cent to population H2 with 4 per cent error margins in both values. This suggests that, on average, one sixth of the lens objects in our sample belongs to the second population with shallower cusp slope. We performed a Monte Carlo study in order to find out the rejection probability for the second population hypothesis. The result suggests that the probability for the second population signature being noise induced is at order of ~ 1 per cent.

As our Monte Carlo testing in section 4 pointed out, the profiles with shallower cusp slopes are more easily perturbed by error sources. These deviations have tendency to make the acquired cusp slope steeper than it really is. Although this is partly reflected by rather wide error range in the population H2 values, our referred population H2 results should be interpreted with caution. The cusp slope value α_{H2} can be alleged as an estimate for the lower limit of the population H2 profiles.

The foremost alternative explanation for the H2 population is that they are actually unresolved triple image lenses. However, this scenario has several weaknesses: the fused pair of images should possess a strong autocorrelation in brightness variations that is equal to the time delay between the images. These unresolved lenses would increase the total number of the triple image lenses and their corresponding statistical frequency to such level that would contradict the acquired cusp slope for the main population H1. If the H2 lenses were unresolved triple image lenses in H1, the share of triple image lenses would be 11 out of 100, and the main population should have profile $\alpha \approx -1.89$ according to the equation (24). This is well off from the determined profile value for the main population. Furthermore, although the H2 population of halos is smaller, they produce distribution that is consistent with the model. This should not be the case if they were triple image lenses – their distribution should be more random.

According to the conventional wisdom acquired from the cosmological N-body simulations, the universal cusp slope for the dark matter haloes is around $\alpha \sim -1.0 \dots -1.5$, depending on the author. However, observations on rotation curves of normal and LSB galaxies suggest even higher values, exceeding $\alpha = -1.0$. Our results contradict most of

these results. The lens density profiles has also been studied by Gavazzi et al. (2007). They used a power law profile with joint weak and strong lensing modelling, and confirmed the SIS lens population (H1), but did not observe the shallower profile population H2. The weak lensing does not have very good resolution, and the pure power law profiles do not account the projected halo component outside the scaling radius r_s realistically. Additionally, they study average properties of 22 lens halos. According to our results, three or four lenses in their sample should have shallower profiles. The second population signature can easily be lost into the residual noise when considering average properties of their lensing sample.

Interestingly, Gustafsson, Fairbairn & Sommer-Larsen (2006) and Romano-Díaz et al. (2008) have performed cosmological N-body simulations with baryonic matter component. They have found similar populations for the halo profiles as we do in our lens study. In the first population, the halo profile is made steeper by the rich baryonic content, down to the value $\alpha \sim -1.9$, which is close to the isothermal value. They also discovered a second population of haloes that were poor in baryonic content, with cusp value $\alpha \sim -1.3$. It would seem, that although baryonic matter density is much lower than density of dark matter, it can still have non-negligible effects on the evolution of dark matter.

Our numerical values are also supported by the additional results discussed in appendix A and the section 2.1. Flat cores $\alpha > -1$ are very poor in strong lensing, and shallow profiles $\alpha \gtrsim -1.5$ should produce excessive number of triple image lenses.

The CSL concept has clear advantages. The method uses more realistic lensing model inspired by N-body simulations. The only required data is sampled double image lens photometry. The method can separate intrinsic properties of the lensing halos from the extrinsic lensing conditions. Thus no information on the lens and the source redshifts, the lens masses or concentrations, cosmology, or theoretical distribution functions characterizing the lens and source populations is needed. This removes many uncertainties that are usually present in the statistical lensing studies.

The method has also disadvantages. When general properties of dark matter haloes are considered, there is a strong selection bias in our study. Our results concern only those haloes that are able to do strong lensing, i.e. haloes with cusp slopes steeper than $\alpha \sim -1$. Generally, the lens objects are massive elliptical or early type galaxies residing at the core of a small galaxy cluster which would incorporate the dark matter halo of the whole cluster into the lensing potential. These kinds of objects are very different from the late type spiral galaxies or LSB-galaxies, which usually cannot perform strong lensing at all. Additionally, there are relatively few observed double image lenses at the moment, and the CSL method requires a hand-picked sample of relatively unperturbed lens systems exhibiting axial symmetry.

New lens systems are found all the time. Certain proportion of these are double image lenses. Larger data-set produces better results, making the CSL analysis more accurate in the future.

ACKNOWLEDGMENTS

The author would like to acknowledge stimulating discussions with Pekka Heinämäki, Pasi Nurmi and Pertti Rautiainen on the key topics in this paper. The author thanks also Marja Annala for her support and help throughout the development of this work. Jussi Alarauhio and Kari Rumukainen are thanked for carefully reading and commenting an early version of this paper. The referee is thanked for the constructive comments on this manuscript. The work of the author has been supported in part through graduate student funding of the University of Oulu. We are grateful for the funding provided by the Magnus Ehrnrooth foundation. This research has made use of the NASA Astrophysics Data System.

REFERENCES

- Abdelqader, M. & Melia, F. 2008, MNRAS, 388, 1869.
- Argo, M. K. et al. 2003, MNRAS, 338, 957.
- Austin, C. G., Williams, L. L. R., Barnes, E. I., Babul, A. J. & Julianne, J. 2005, ApJ, 634, 756.
- Beacom, J. F., Bell, N. F. & Mack, G. D. 2007, Phys. Rev. Lett., 99, 231301.
- Biggs, A. D. et al. 2003, MNRAS, 338, 1084.
- Bicker, J., Alvensleben, U. F.-v., Möller, C. S. & Fricke, K. J. 2003, A&A, 413, 37.
- Blumenthal, G. R., Faber, S. M., Primack, J. R., & Rees, M. J. 1984, Nature, 311, 517.
- Bolton, A. S. et al. 2006, ApJ, 638, 703.
- Borzumati, F., Bringmann, T. & Ullio, F. 2008, Phys. Rev. D, 77, 063514.
- Browne, I. W. A., Wilkinson, P. N., Patnaik, A. R. & Wrobel, J. M. 1998, MNRAS 293, 257.
- Buote, D. A., Lewis, A. D., Brighenti, F. & Mathews, W. G. 2003, ApJ, 594, 741.
- Burkert, A. 1995, ApJ, 447, L25.
- Burkert, A. 2000, ApJ, 534, L143.
- Chemin, L. & Hernandez, O. 2009, A&A, 499, L25.
- Cheng, H.-C., Feng, J. L., & Matchev, K. T. 2002, Phys. Rev. Lett., 89, 211301.
- Dalal, N. & Kochanek, C. S. 2002, ApJ, 572, 25.
- Davis, M., Efstathiou, G., Frenk, C. S., & White, S. D. M. 1985, ApJ, 292, 371.
- Debatista, V. P. & Sellwood, J. A. 2000, ApJ, 543, 704.
- Dehnen, W. & McLaughlin, D. E. 2005, MNRAS, 363, 1057.
- Donato, F. et al. 2009, arXiv:0904.4054.
- D'Onghia, E. & Burkert, A. 2003, ApJ, 586, 12.
- D'Onghia, E., Firmani, C. & Chincarini, G. 2003, MNRAS, 338, 156.
- Dubinski, J., Berentzen, I., & Shlosman, I. 2009, ApJ, 697, 293.
- Eigenbrod, A., Courbin, F., Meylan, G., Vuissoz, C. & Magain, P. 2006, A&A, 451, 759.
- Ellis, J., Kelley, S., & Nanopoulos, D. V. 1991, Phys. Lett. B, 260, 131.
- Elmegreen, B. G. & Elmegreen, D. M. 1985, ApJ, 288, 438.
- Gao et al. 2004 MNRAS, 355, 819.
- Gavazzi, 2005 A&A, 443, 793.

- Gavazzi, R. et al. 2007, *ApJ*, 667, 176.
- Ghigna, S., Moore, B., Governato, F., Lake, G., Quinn, T. & Stadel, J. 2000, *ApJ*, 544, 616.
- Greenfield, P. E., Roberts, D. H. & Burke, B. F. 1985, *ApJ*, 293, 370.
- Gustafsson, M., Fairbairn, M. & Sommer-Larsen, J. 2006, *Phys. Rev. D*, 74, 123522.
- Hagen, H.-J. & Reimers, D. 2000, *A&A*, 357, L29.
- Hansen, S. H. 2009, *ApJ*, 694, 1250.
- Hayashi, E., Navarro, J. F. & Springel, V. 2007, *MNRAS*, 377, 50.
- Hooper, D., Finkbeiner, D. P. & Dobler, G. 2007, *Phys. Rev. D*, 76, 083012.
- Humphrey, Buote, D. A., Gastadello, F., Zappacosta, L., Bullock, J. S., Brighenti, F. & Mathews, W. G. 2006, *ApJ*, 646, 899.
- Humphrey, P. J., Liu, W. & Buote, D. A. 2009, *ApJ*, 693, 822.
- Huterer, D., Keeton, C. R. & Ma, C.-P. 2005, *ApJ*, 624, 34.
- Inada, N. et al. 2005, *AJ*, 130, 1967.
- Jackson, N. et al. 1995, *MNRAS*, 274, L25.
- Jackson, N., Xanthopoulos, E. & Browne, I. W. 2000, *MNRAS*, 311, 389.
- Johnston, D. E. et al. 2003, *AJ*, 126, 2281.
- Jørgensen, I., Franx, M. & Kjærgaard, P. 1995, *MNRAS*, 273, 1097.
- Koopmans, L. V. E. et al. 1999, *MNRAS*, 303, 727.
- Koopmans, L. V. E. et al. 2000, *A&A*, 361, 815.
- Lacy, M., Gregg, M., Becker, R. H., White, R. L., Glikman, E., Helfand, D. & Winn, J. N. 2002, *AJ*, 123, 2925.
- Lehár, J. et al. 2000, *ApJ*, 536, 584.
- Limousin, M. et al. 2008, *A&A*, 489, 23.
- Mahdavi, A., Hoekstra, H., Babul, A., Sievers, J., Myers, S. T. & Henry, J. P. 2007, *ApJ*, 664, 162.
- Magain, P., Surdej, J., Vanderriest, C., Pirenne, B. & Hutsemékers, D. 1992, *A&A*, 253, L13.
- Marlow, T. et al. 2001, *AJ*, 121, 619.
- Martin, S. P. 1998, in G. L. Kane, editor, *Perspectives on Supersymmetry*.
- McKean, J. P. et al. 2005, *MNRAS*, 356, 1009.
- Moore, B., Governato, F., Quinn, T., Stadel, J. & Lake, G. 1998, *ApJ*, 499, L5.
- Moore, B., Quinn, T., Governato, F., Stadel, J. & Lake, G. 1999, *MNRAS*, 310, 1447.
- Morgan, D. N., Dressler, A., Maza, J., Schechter, P. L. & Winn, J. N. 1999, *AJ*, 118, 1444.
- Morgan, D. N., Becker, R. H., Gregg, M. D., Schechter, P. L. & White, R. L. 2001, *AJ*, 121, 611.
- Morgan, D. N., Gregg, M. D., Wisotzki, L., Becker, R., Maza, J., Schechter, P. L. & White, R. L. 2003, *AJ*, 126, 696.
- Morgan, D. N., Snyder, J. A. & Reens, L. H. 2003, *AJ*, 126, 2145.
- Muñoz, J. A., Falco, E. E., Kochanek, C. S., Lehár, J., McLeod, B. A., Impey, C. D., Rix, H.-W. & Peng, C. Y. 1998, *Ap&SS*, 263, 51.
- Muñoz, J. A. et al. 2001, *ApJ*, 546, 769.
- Mutka, P. T. & Mähönen, P. H., 2006, *MNRAS*, 373, 243.
- Myers, S. T. et al. 1995, *ApJ*, 447, L5.
- Navarro, J. F., Frenk, C. S. & White, S. D. M. 1996, *ApJ*, 462, 563.
- Navarro, J. F., Frenk, C. S. & White, S. D. M. 1997, *ApJ*, 490, 493.
- Ofek, E. O., Rix, H.-W. & Maoz, D. 2003, *MNRAS*, 343, 639.
- Oguri, M. et al. 2004, *PASJ*, 56, 399.
- Oguri, M. et al. 2005, *ApJ*, 622, 106.
- Patnaik, A. R., Browne, I. W. A., Wilkinson, P. N. & Wrobel, J. M. 1992, *MNRAS* 254, 655.
- Peebles 1982, *ApJL*, 263, L1.
- Pindor, B. et al. 2004, *AJ*, 127, 1318.
- Pindor, B. et al. 2006, *AJ*, 131, 41.
- Poggianti, B. M. 1997, *AASS*, 122, 399.
- Pointecouteau, E., Arnaud, M. & Pratt, G. W. 2005, *A&A*, 435, 1.
- Power, C. et al. 2003, *MNRAS*, 338, 14.
- Randall, S. W., Markevitch, M., Clowe, D., Gonzalez, A. H. & Bradac, M. 2008, *ApJ*, 679, 1173.
- Ratnatunga, K. U., Griffiths, R. E. & Ostrander E. J. 1999, *AJ*, 117, 2010.
- Rautiainen, P., Salo, H., & Laurikainen, E. 2008, *MNRAS*, 388, 1803.
- Romano-Díaz, E., Shlosman, I., Hoffman, Y. & Heller, C. 2008, *ApJ*, 685, L105.
- Romeel, D., Spergel, D. N., Steinhardt, B. D. & Wandelt, B. D. 2001, *ApJ*, 547, 574.
- Rozo, E., Zentner, A. R., Bertone, G. & Chen, J. 2006, *ApJ*, 639, 573.
- Rusin, D. et al. 2001, *AJ*, 122, 591.
- Rusin, D., Norbury, M., Biggs, A. D., Marlow, D. R., Jackson, N. J., Browne, I. W. A., Wilkinson, P. N. & Myers, S. T. 2002, *MNRAS*, 330, 205.
- Sand, D. J., Treu, T. & Ellis, R. S. 2002, *ApJ*, 574, L129.
- Sand, D. J., Treu, T., Smith, G. P. & Ellis, R. S. 2004, *ApJ*, 604, 88.
- Sanderson, A. J. R., Finobuenov, A. & Mohr, J. J. 2005, *ApJ*, 630, 191.
- Schechter, P. L., Gregg, M. D., Becker, R. H., Helfand, D. J. & White, R. L. 1998, *AJ*, 115, 1371.
- Schneider, D. P., Lawrence, C. R., Schmidt, M., Gunn, J. E., Turner, E. L., Burke, B. F. & Dhawan, V. 1985, *ApJ*, 294, 66.
- Schneider, P., Ehlers, J. & Falco, E. E. 1992, *Gravitational Lenses*, Springer.
- Schramm, T. 1990, *A&A*, 231, 19.
- Sellwood, J. A. 2008, *ApJ*, 679, 379.
- Sereno, M., Lubini, M. & Jetzer, Ph. 2009, *arXiv:0904.0018*.
- Servant, G. & Tait, T. M. P. 2003, *Nuclear Physics B*, 650, 391.
- Spergel, D. N. & Steinhardt, P. J. 2000, *Phys. Rev. Lett.*, 84, 3760.
- Subrahmanyam, R., Narasimha, D., Rao, A. P. & Swarup, G. 1990, *MNRAS*, 246, 263.
- Surdej, J. et al. 1988, *A&A*, 198, 49.
- Surdej, J., Claeskens, J.-F., Remy, M., Refsdal, S., Pirenne, B., Prieto, A. & Vanderriest, C. 1997, *A&A*, 327, L1.
- Timmer, J. & König, M. 1995, *A&A*, 300, 707.
- Toft, S., Hjorth, J. & Burud, I. 2000, *A&A*, 357, 115.
- Valenzuela, O., et al. 2007, *ApJ*, 657, 773.
- Vanden Berk, D. E. et al. 2004, *ApJ*, 601, 692.
- Vikhlinin, A., Kravtsov, A., Forman, W., Jones, C., Markevitch, M., Murray, S. S. & Van Speybroeck, L. 2006, *ApJ*,

640, 691.

- Voigt, L. M. & Fabian, A. C. 2006, MNRAS, 368, 518.
 Weinberg, M. D. 1985, MNRAS, 213, 451.
 Weinberg, M. D. & Katz, N. 2007, MNRAS, 375, 425.
 Wilkinson, P. N., Browne, I. W. A., Patnaik, A. R., Wrobel, J. M. & Sorathia, B. 1998, MNRAS, 300, 790.
 Winn, J. N. et al. 2000, AJ, 120, 2868.
 Winn, J. N., Hewitt, J. N., Patnaik, A. R., Schechter, P. L., Schommer, R. A., López, S., Maza, J. & Wachter, S. 2001, AJ, 121, 1223.
 Winn, J. N. et al. 2002, AJ, 123, 10.
 Wisotzki, L., Köhler, T., Kayser, R. & Reimers, D. 1993, A&A, 278, L15.
 Wisotzki, L., Schechter, P. L., Chen, H.-W., Richstone, D., Jahnke, K., Sánchez, S. F. & Reimers, D. 2004, A&A, 419, L31.
 Wucknitz, O., Wisotzki, L., Lopez, S. & Gregg, M. D. 2003, A&A, 405, 445.
 Wyithe, J. S. B. & Loeb, A., 2002, ApJ, 577, 57.
 Xanthopoulos, E. et al. 1998, MNRAS, 300, 649.
 York, T. et al. 2005, MNRAS, 361, 259.
 Zackrisson, E., Bergvall, N., Marquart, T. & Östlin, G. 2006, A&A, 452, 857.
 Zhao, H. 1996, MNRAS, 278, 488.

APPENDIX A: CUSP SLOPE LIMIT FOR STRONG LENSING

Our previously published lensing theory in Mutka & Mähönen (2006) approximates the surface density κ produced by the GNFW mass profile with

$$\kappa = ax^{\alpha+1} + b, \quad (\text{A1})$$

where constants a and b depend only on the cusp slope value α of the profile. The radial coordinate x on the lens plane and similar coordinate y on the source plane are defined as in Schneider, Ehlers & Falco (1992). Corresponding unnormalized lens equation is ($\alpha \neq -1$)

$$y = x - \frac{\mu_0}{x} \left(\frac{a|x|^{\alpha+3}}{(\alpha+3)} + \frac{b}{2}|x|^2 \right). \quad (\text{A2})$$

Here $\mu_0 = 4\rho_0 r_s / \Sigma_{\text{cr}}$ is the normalized projected density. This lens equation has its Einstein radius at $y = 0$, i.e.

$$x = x_e = \left[\frac{\alpha+3}{\mu_0 a} \left(1 - \frac{\mu_0 b}{2} \right) \right]^{1/(\alpha+1)}, \quad (\text{A3})$$

where $\mu_0 = 4\rho_0 r_s / \Sigma_{\text{cr}}$. Here the scale radius is

$$r_s = \frac{1}{c_1} \left\{ \frac{3M}{800\pi\rho_{\text{cr}}} \right\}^{1/3}, \quad (\text{A4})$$

where M is the total mass of the lens and c_1 the profile concentration. The central density is

$$\rho_0 = \frac{200c_1^3 \rho_{\text{cr}}}{f(c_1)}, \quad (\text{A5})$$

where

$$f(c_1) = \int_0^{c_1} dx x^{\alpha+2} (1+x)^{-(\alpha+3)}. \quad (\text{A6})$$

In the previous equations, the critical density ρ_{cr} is defined as

$$\rho_{\text{cr}} = \frac{3H_0^2}{8\pi G} [\Omega_m(1+z_L)^3 + \Omega_R(1+z_L)^2 + \Omega_\Lambda]. \quad (\text{A7})$$

and the critical surface density is

$$\Sigma_{\text{cr}} = \frac{c^2 D_s}{4\pi G D_L D_{LS}}. \quad (\text{A8})$$

In equations (A7) and (A8) the Hubble constant is H_0 , the gravitational constant is G and the speed of light is c . Subscripts L and S refer to the lens and the source, and symbol D to corresponding angular cosmological distance and z to redshift. The total energy density of the universe is parametrized with Ω_m , Ω_R and Ω_Λ (matter, curvature and cosmological constant).

At the limit where the lens cannot produce multiple images, the Einstein radius is reduced to zero and becomes imaginary. Thus, a condition for strong lensing can be acquired from the equation (A3) as

$$\mu_0 < \frac{2}{b}. \quad (\text{A9})$$

This equation can be solved numerically with the definitions presented above, but it can also be approximated with

$$b \approx (\alpha+1)^{-1}(\alpha+2)^{-1} \quad (\text{A10})$$

and

$$f(c_1) = f(c_1; \alpha) \approx f(c_1; -1) = \log(1+c_1) - \frac{c_1}{1+c_1} \quad (\text{A11})$$

with good accuracy when $\alpha > -1$. When these approximations are inserted into the condition (A9), we can solve the maximum cusp slope for the strong lensing as

$$\alpha = \alpha_{\text{sl}} = -\frac{3}{2} + \frac{1}{2} \sqrt{1 + \frac{1600r_s \rho_{\text{cr}} c_1^3 (1+c_1)}{3\Sigma_{\text{cr}} [(1+c_1) \log(1+c_1) + c_1]}}. \quad (\text{A12})$$